Journal of Materials Chemistry C

Self-assembled multiferroic perovskite-spinel nanocomposite thin films: Epitaxial growth, templating and integration on Silicon

Journal:	*Journal of Materials Chemistry C*
Manuscript ID	TC-REV-04-2019-002033.R1
Article Type:	Review Article
Date Submitted by the Author:	29-Jun-2019
Complete List of Authors:	Kim, Dong Hun; Myongji university, Department of materials science and engineering Ning, Shuai; Massachusetts Institute of Technology, Ross, Caroline; MIT,

Self-assembled multiferroic perovskite-spinel nanocomposite thin films: Epitaxial growth, templating and integration on Silicon

Dong Hun Kim[1,*], Shuai Ning[2], and Caroline A. Ross[2]

[1] Department of Materials Science and Engineering, Myongji University, Yongin, Republic of Korea

[2] Department of Materials Science and Engineering, Massachusetts Institute of Technology, Cambridge, Massachusetts, 02139, USA

[*)] Author to whom correspondence should be addressed. Electronic mail: dhkim@mju.ac.kr

Abstract

This review describes recent progress in the growth and properties of self-assembled multiferroic perovskite-spinel nanocomposite thin films, in particular, $BiFeO_3$-$CoFe_2O_4$, and their integration on silicon or pre-patterned substrates. Vertically aligned nanocomposite thin films, in which ferromagnetic spinel $CoFe_2O_4$ nanopillars grow in a ferroelectric perovskite $BiFeO_3$ matrix, have been investigated for applications such as next generation memory devices. The strain transfer between the two oxide phases at the vertical interface enables cross-coupling of the properties, i.e. a magnetic (electric) field can modify the polarization (magnetization) state, making the nanocomposite a two-phase magnetoelectric multiferroic. The ability to grow high quality thin film nanocomposites and the control of their properties through epitaxial strain transfer are prerequisites for their incorporation into practical devices. Most work has been carried out on perovskite substrates using pulsed laser deposition, and integration on semiconductor-compatible substrates using scalable deposition processes presents a challenge. This review focuses on the epitaxial integration of $BiFeO_3$-$CoFe_2O_4$ nanocomposite thin films using sputter deposition on silicon substrates, and discusses recent work on the formation of highly ordered nanocomposites using various template patterning methods. This robust, scalable route for large-area fabrication of multifunctional oxide nanocomposites using sputtering brings the exciting prospects offered by these materials closer towards technological realization.

1. Introduction

The exponentially growing amount of data in cloud storage and big data platforms has generated a new need for more advanced technology in memory and information storage. The limitations in scalability of NAND flash memories and DRAMs (dynamic random access memories) has motivated a search for new memories operating on qualitatively different principles. [1-5] Memory technology has been based on charge storage in semiconductor devices, polarization in dielectrics or ferroelectrics, or magnetization direction in ferromagnets. In the latter two examples, ferroelectric random access memory (FeRAM) and magnetic random access memory (MRAM), the direction of electric or magnetic dipoles inside the material can be changed with an external electric field or a magnetic field respectively to encode a data bit. FeRAM and MRAM are nonvolatile memories that can maintain information even if power is not supplied to the memory element because the direction of the dipole is not changed unless an external electric field or a magnetic field is applied after information is written. [6-9] FeRAM has the advantages of being able to record information at high speed with low power but it has the disadvantage of integration challenges, a slow reading speed, and limited endurance. While MRAM is highly integrated, its power consumption can be high. Devices based on multiferroic materials have been proposed as a next-generation memory, inspiring the search for multiferroic materials with coexisting ferromagnetic and ferroelectric order. [10-12] In magnetoelectric multiferroics, an applied magnetic field can change the electric polarization and an electric field can change the magnetization. A variety of electrical and magnetic states can potentially be formed in a single storage location to create a multi-bit memory device.

Vertically aligned epitaxial oxide nanostructures formed by the growth of two immiscible oxide phases are attractive candidates for two-phase multiferroics. [13-15] The most widely studied examples are perovskite-spinel magnetoelectric nanocomposites such as $BiFeO_3$-$CoFe_2O_4$ (BFO-CFO), which typically consist of nanoscale pillars of the ferrimagnetic CFO phase inside a matrix of the ferroelectric BFO phase grown on a (001) oriented cubic single crystal perovskite substrate. These nanocomposites can exhibit perpendicular magnetic anisotropy if the CFO is under compression along the vertical direction or if the pillar aspect ratio is sufficiently high.

Self-assembled perovskite-spinel nanostructures have been investigated in detail following reports that the magnetic state could be electrically controlled. [15-17] The nanocomposites have a large interfacial area between the CFO (magnetostriction constant, $\lambda_{100,\ CFO} = (-250 \text{ to } -590) \times 10^{-6}$) [18] and BFO (piezoelectric coefficient, $d_{33,\ BFO} \approx 60$ pm V^{-1}) [19] which leads to coupling between the magnetic and ferroelectric order parameters via strain transfer. The epitaxial interface between the magnetostrictive and piezoelectric materials along the vertical (out-of-plane) direction provides a means to control the elastic strain in the two components, thus allowing tuning of the stress-induced magnetic anisotropy and ferroelectric properties. [20-24]

In order to take advantage of both ferroelectricity and magnetism of nanocomposites for memory devices, ordering of the CFO nanopillars at specific locations on the substrate is desirable. Recent advances in patterning or templating methods using anodic aluminum oxide (AAO), focused ion beam (FIB), electron beam (e-beam), and triblock terpolymer templates have made it possible to obtain highly ordered nanocomposites by controlling the nucleation of the CFO nanopillars. [25-28] Furthermore, efforts to integrate self-assembled epitaxial oxides on silicon (Si) substrates are underway using deposition processes that are compatible with large-scale manufacturing.

In this review article, section 2 gives a brief overview of multiferroics, especially self-assembled epitaxial multiferroic nanocomposite thin films and the contribution of strain to magnetic anisotropy. In section 3, we introduce recent progress in nanocomposites grown using pulsed laser deposition (PLD) including the growth mechanism and magnetic property modulation. We focus section 4 on nanocomposite growth using sputtering and its integration on Si substrates and on ordered templates for low cost and large area applications.

2. Multiferroic thin films

2.1. Two-phase multiferroic nanocomposite thin films

The limitations of single-phase multiferroics, i.e. the lack of materials exhibiting both room temperature ferroelectricity and ferromagnetism, may be overcome by using two-phase multiferroics, artificially synthetized composites comprising a ferromagnetic, ferrimagnetic or antiferromagnetic phase and a ferroelectric phase which are coupled by strain. Application of an electric field leads to a piezoelectric strain in the ferroelectric phase which is transmitted to the magnetic phase, leading to a magnetoelastic contribution to the anisotropy and a change in magnetization; on the other hand a magnetic field causes a magnetoelastic strain which couples to the ferroelectric phase leading to a change in polarization. The implementation of devices using these composite materials is facilitated by their high ME coefficient (α_E, units: V/cm·Oe) which characterizes the effect of an applied magnetic field on electric polarization or electric field on magnetization. Characterization of α_E is often performed by measuring piezoelectric response at small applied magnetic fields, but changes in magnetic coercivity or anisotropy field can also be performed. The different methods and definitions used to obtain ME coefficients presents a challenge in comparing the performance and utility of magnetoelectric materials of different compositions, geometries and processing routes.

Research on multiferroic composites originated in powder and bulk samples, but considerable attention has recently been focused on thin film composites. Advances in thin film growth techniques

have enabled the fabrication of a variety of two-phase nanostructures by controlling the composition, microstructure, interface state, and strain of the material, and the resulting magnetic, ferroelectric, and ME properties. Nanocomposite thin films can be categorized into three different types based on the geometry of the phases: 0-3 type (nanoparticles within a continuous matrix), 2-2 type (bilayer or multilayer thin films), and 1-3 type (aligned nanorods or nanopillars within a continuous matrix).

In the 0-3 type multiferroic nanocomposite, magnetic nanoparticles such as CFO, $NiFe_2O_4$ (NFO), or $La_{0.6}Ca_{0.4}MnO_3$ are dispersed within a ferroelectric matrix such as $PbZrTiO_3$ (PZT), BTO, or $Bi_{0.6}Nd_{0.4}TiO_3$. Zhai *et al.* reported a large ME coefficient of 80 mV/cm·Oe in a 0.32NFO-0.68$PbZr_{0.57}Ti_{0.43}O_3$ composite ceramic fabricated by conventional oxide sintering. [29] Wan *et al.* investigated polycrystalline CFO-$PbZr_{0.52}Ti_{0.48}O_3$ (PZT) nanocomposite films fabricated by a sol-gel method in which CFO nanoparticles were embedded in the PZT matrix, and obtained an ME coefficient of 220-317 mV/cm·Oe. [30] A nanocomposite thin film in which NFO nanoparticles were embedded in a PZT matrix was prepared on Nb-doped $SrTiO_3$ (Nb:STO) substrates using PLD, exhibiting maximum transverse and longitudinal ME coefficients of 4 and 16 mV/cm·Oe respectively. [31] The smaller coefficients in the nanocomposite thin film compared with the bulk particulate composites are attributed to substrate clamping effects. Zhong *et al.* found ferroelectric and ferromagnetic behaviors and an ME coefficient of ~34.5 mV/cm·Oe in $Bi_{3.15}Nd_{0.85}Ti_3O_{12}$-CFO polycrystalline films. [32] McDannald *et al.* fabricated 0-3 type nanocomposite films using spin coating in which CFO nanoparticles of 5-8 nm diameter were dispersed in a PZT matrix. The nanocomposites exhibited high transverse and longitudinal ME coefficients of 549 and 338 mV/cm·Oe, respectively. [33] These 0-3 type nanocomposite films are straightforward to synthesize but it is hard to polarize the ferroelectric phase even in a large electric field due to a significant leakage current. Li *et al.* fabricated a CFO/BFO nanocomposite heterostructure by alternately growing 2-2 and 1-3 type composite layers. The heteroepitaxial films not only overcame the clamping effect from the substrate, but also suppressed the leakage current through the ferromagnetic phase. [34]

The 2-2 type multiferroic nanocomposite thin films are formed by stacking two or more layers of ferromagnetic and ferroelectric materials. They typically have lower leakage current than 0-3 type nanocomposites, but clamping from the substrate limits the strain that can be developed in-plane. [20] However, 2-2 type nanocomposite thin films have been investigated widely. They can be made by growth of an epitaxial ferroelectric (ferromagnetic) thin film on a ferromagnetic (ferroelectric) single crystal substrate, e.g. a ferroelectric PZT film on a single crystal LSMO, [35] or an epitaxial magnetic $LaCa(Sr)MnO_3$ film on a ferroelectric single crystal BTO or $Pb(Mg,Nb)O_3$-$PbTiO_3$. [36-37] Wang *et al.* grew a BTO thin film directly on a CFO ceramic, obtaining an ME coefficient of about 38 mV/cm·Oe,

which is one order of magnitude lower than that for the epitaxial analog. [38] PZT/$Ni_{0.8}Zn_{0.2}Fe_2O_4$ (NZFO) bilayers, PZT/NZFO/PZT trilayers, Fe_3O_4 films on BTO substrates, and PZT/$La_{0.7}Sr_{0.3}MnO_3$ (LSMO) bilayer nanocomposites exhibit coexisting ferroelectric and ferromagnetic properties. [39-41] Ortega *et al.* [42] investigated ME coupling of PLD grown CFO/PZT multilayers from the change in ferroelectric hysteresis loop due to a magnetic field. Zhang *et al.* reported a 2-2 heterostructure of CFO/BTO thin films grown on a (001) STO substrate with an ME coefficient of ~66 mV/cm·Oe. [43] He *et al.* inserted buffer and bottom electrode layers of $LaNiO_3$ (LNO) film in a PZT/CFO bilayer film to relax the clamping effect from the substrate and thereby enhance the ME response. [44] By choosing a Ni foil substrate a much larger ME coefficient of 772 mV/cm·Oe was obtained due to lower substrate clamping. [45] Mundy *et al.* reported ferroelectricity and magnetic ordering near room temperature within $(LuFeO_3)_m/(LuFe_2O_4)_1$ superlattices. [46] Overall, although 2-2 nancomposites are convenient to fabricate, their ME values are limited by substrate clamping.

The 1-3 type nanocomposite thin films are exemplified by a vertically aligned nanostructure (VAN) in which ferromagnetic nanopillars grow epitaxially with an immiscible ferroelectric matrix, or ferroelectric pillars in a ferromagnetic matrix. The substrate clamping effect is less than that of the 2-2 type and the 1-3 type is therefore expected to show a larger ME coefficient. Ramesh *et al.* described a 1-3 type BTO-CFO nanocomposite [15] in which CFO nanopillars were embedded in a BTO matrix. The film showed both ferroelectric polarization and a uniaxial magnetic anisotropy with out-of-plane easy axis, and a magnetization change was observed around the phase transition temperature of BTO unlike in the CFO/BTO multilayer, indicating a significant ME coupling in the nanocomposite. Since this pioneering work, there have been several other studies on the growth mechanism, magnetic, ferroelectric, and ME properties of BTO-CFO nanocomposite thin films. [47-50]

The BFO-CFO VAN has attracted the most study due to its larger ME coupling. Ramesh *et al.* investigated the electric field control of magnetization using magnetic force microscopy in electrically-poled films. [24, 51] The static perpendicular ME susceptibility, $\alpha_{E33} = \Delta M/\Delta E$, where ΔM is the electrically-induced magnetization change and ΔE is the poling field was 0.01 cm·Oe/V. Wang *et al.* grew BFO-CFO nanocomposite films on piezoelectric $Pb(Mg_{1/3}Nb_{2/3})_{0.7}Ti_{0.3}O_3$ (PMN-PT) (001) substrates and showed a dramatic decrease of the out-of-plane remanent magnetization depending on the applied electric field. [23] Yan *et al.* observed the direct ME coupling effect in a BFO-CFO nanocomposite on conductive $SrRuO_3$ (SRO)-buffered STO (001) substrates using a magnetic cantilever method and the maximum ME coefficient was 18 mV/cm·Oe. [52] Oh *et al.* revealed that the transverse ME coefficient was five times larger than the longitudinal ME coefficient in a 300 nm thick BFO-CFO nanocomposite film due to preferred magnetic domain alignment along the [001] direction coming from compressive strain. [53]

Besides the BFO-CFO and BTO-CFO systems, many other 1-3 type nanocomposite thin films consisting of spinel and perovskite phases have been developed, including PZT-CFO or $PbTiO_3$-CFO, [54-57] BFO-$MgFe_2O_4$ (MFO), [58] BFO-NFO, [59] and $Sr(Ti_{1-x}Fe_x)O_3$-CFO. [60]

2.2. Strain mediated ME effects

ME coupling in two-phase multiferroics originates from strain transfer between the two phases. This is illustrated for 1-3 nanocomposites in **Figure 1**, where the polarization (magnetization) is changed by a magnetic (electric) field. The ME effect in composite materials is a product tensor property, a result of the product of the magnetostrictive or magnetoelastic effect (coupling between magnetization and lattice strain) in one phase and the piezoelectric effect (coupling between polarization and lattice strain) in the other phase. [61] The ME coupling is characterized by measuring the direct or converse ME coefficient. [62] The direct ME effect detects an electrical signal resulting from a magnetic field. Strain generated in the magnetostrictive phase under a magnetic field induces surface charges in the piezoelectric phase. A static magnetic field superimposed with a small ac magnetic field (ΔH_{ac}) is applied to the nanocomposite and the surface charge or voltage signal is recorded. The direct ME voltage coefficient is given by $\alpha_E = \Delta E / \Delta H_{ac}$. Another way to estimate ME coupling strength is using the magnetocapacitance effect which is a combination of magnetoresistive and interfacial capacitive effects. The magnetocapacitance of vertically aligned BFO-CFO nanocomposite thin film was about 0.9 μC/cm·Oe. [25]

The converse ME effect enables the modulation of magnetization by electric field. Strain in the piezoelectric phase under an electric field induces a magnetization change in the ferromagnetic phase. This is particularly useful for designing nonvolatile memories. To measure the converse ME effect, an electric field is applied to the ME nanocomposites and the change of magnetization is detected. This can be accomplished using vibrating sample magnetometry, ferromagnetic resonance, superconducting quantum interference device magnetometry, the magneto-optic Kerr effect, and x-ray absorption near edge spectroscopy.

The vertically aligned nanocomposites, in which magnetic CFO pillars grew coherently with a ferroelectric BFO matrix, are excellent systems for taking advantages of strain engineering while reducing substrate clamping. CFO has a large magnetostriction which can dominate the magnetic anisotropy, and BTO or BFO exhibit a strong piezoelectric response, making these preferred materials for ME nanocomposites. In VANs of BFO-CFO or BTO-CFO grown on (001) STO substrates, the effect of lattice strain due to the vertical interfaces is evident from the magnetic anisotropy of the CFO. The lattice

mismatch between the two phases leads to a strong magnetic anisotropy with out-of-plane easy axis. The magnetoelastic anisotropy field is estimated by $H_{me} = \frac{3\lambda_{001} Y \varepsilon_{001}}{M_s}$, where λ_{001} is the magnetostriction coefficient (-250 to -590) × 10^{-6}), [18] Y is Young's modulus (141.6 GPa) [63], ε_{001} is the vertical compressive strain and M_s is the saturation magnetization of CFO of 400 emu cm^{-3}. [64]. This dominates the shape anisotropy field H_{sh} given by $4\pi \cdot (N_x - N_z) \cdot M_s$, where N_x and N_z are demagnetizing factors along in-plane and out-of-plane directions. Magnetocrystalline anisotropy does not contribute to the difference between in-plane [100] or [010] and out-of-plane [001] response of the pillars. The magnetic anisotropy field from experiments is well matched to the expected magnetoelastic anisotropy [17, 64-67] which supports the primary role of magnetoelastic anisotropy. This was confirmed by the measurement of anisotropy in thinner films, where the substrate clamping determines the strain. [67] Scanning probe microscopy was used to show that the magnetization of about half of the CFO pillars could be reversed by locally applying a voltage after saturating the magnetization of the pillars in one direction. This was attributed to a strain induced rotation of the magnetic anisotropy of the pillars upon application of an electric field to the surrounding ferroelectric matrix. [24, 51]

2.3. Multiferroic nanocomposites for new memories

The discovery and development of multiferroic materials enables new types of memory devices. Multiferroic materials may allow the realization of four-state logic in a single device whereas FeRAM and MRAM use only the ferroelectric polarization and magnetization, respectively. [10-11, 68-69] Moreover, the electrical control of magnetization or magnetic control of polarization via ME coupling offers a new opportunity to combine the advantages of FeRAM and MRAM in the form of non-volatile magnetic storage.

Several ME device concepts have been introduced. Bibes and Barthélémy proposed a magnetoelectric random access memory (MERAM) relying on magnetoelectric and interfacial exchange coupling between a single phase multiferroic material such as BFO and a ferromagnet. The magnetization of the ferromagnetic layer can be switched by applying a voltage rather than a large current or magnetic field. [70] Mankalale *et al.* suggested a spintronic logic device denoted as CoMET (Composite-input Magnetoelectric-based Logic Technology) based on magnetoelectric coupling and current-driven domain wall propagation. The composite input structure included a ferromagnet with an in-plane magnetic anisotropy on a ferromagent with a perpendicular magnetic anisotropy. [71] Manipatruni *et al.* reported a magnetoelectric spin-orbit (MESO) device that includes a magnetoelectric switching capacitor and

topological material. The scalable transduction mechanism consists of ferroelectric/magnetoelectric switching and topological conversion of spin to charge. [72]

Wolf *et al.* introduced a ME memory called reconfigurable array of magnetic automata (RAMA) based on magnetic quantum cellular automata (MQCA) arrays made of 1-3 type ME nanocomposite thin films. [73] Magnetic spinel pillars in a ferroelectric perovskite matrix are configured in a cross bar array structure consisting of orthogonal metal wires, and the pillar positions and the wires are defined by nanoscale lithography or polymeric self-assembly methods. The nanopillars are magnetized out of plane, and the magnetization is reoriented in-plane by application of a local electric field. [51] Each bit is represented by four pillars in a square, coupled magnetostatically to have alternating magnetization directions, and magnetostatic interactions between bits enable data to be propagated and logic operations conducted analogously to quantum cellular automata logic based on charged arrays of semiconductor quantum dots. MQCA logic has been demonstrated in patterned magnetic systems [74], but realization of practical devices is hampered by the inability to control the direction of propagation of data, and switching field distributions which disrupt the magnetostatic coupling. [75]

3. Self-assembled growth and physical properties tuning of perovskite-spinel nanocomposites grown by PLD

3.1. PLD-grown spinel and perovskite films

PLD is a versatile film deposition technique for the growth of complex oxide films including epitaxial films, heterostructures and superlattices, and VANs. A high-power pulsed laser beam is focused onto a target that is usually rotated, or rastered, in order to avoid local erosion by repeated ablation. The ejected species expand into the surrounding vacuum or gas ambient in the form of a plume containing energetic species including atoms, molecules, electrons, ions, clusters, and particulates, which impinge on the substrate. [76-77]

PLD has been used extensively for making perovskite and spinel oxides, both as single phase films and as components of magnetoelectric VANs. In the case of BFO, epitaxial films grown by PLD at 670 °C substrate temperature in 100-200 mTorr of oxygen pressure [19, 78-79] exhibited larger polarization than that of bulk BFO, attributed to the epitaxial strain and low leakage in the films. The measured value of ~90 $\mu C/cm^2$ along the [111] direction of the pseudo-cubic perovskite unit cell is consistent with the theoretical value of 90–100 $\mu C/cm^2$ calculated by density functional theory. [80] There has been considerable research on enhancing the remnant polarization of epitaxial BFO thin films and controlling crystal structure and domain state. Bulk BFO exhibits a rhombohedral unit cell with

polarization along <111>, but the structure and its associated ferroelectric properties can be varied when BFO is grown epitaxially on different perovskite substrates. STO substrates typically yield rhombohedral BFO with a small monoclinic distortion (R-like BFO) which polarizes along <111>. [81-87] On the other hand, $LaAlO_3$ (LAO) substrates yield an epitaxially stabilized tetragonal BFO denoted as T-like BFO which has c/a ≈ 1.25–1.3. T-like BFO is polarized along [001] and exhibits a simpler switching process with higher remnant polarization. [81-85, 88-91]

For CFO, Dorsey *et al.* and Lisfi *et al.* reported a reorientation of the magnetic anisotropy of PLD-grown CFO on (001) MgO substrates by varying the growth temperature (200-800 °C) and film thickness (60-400 nm). [92-93] Hu *et al.* demonstrated that magnetic behavior in epitaxial CFO films grown at 400 °C in 7mTorr O_2 is governed by lattice strain. [94] There have been several reports on substrate effects on film properties, such as the change in magnetic anisotropy due to strain state for films grown on MgO and STO substrates which impose in-plane tensile strain and compressive strain, respectively. [95-100]

3.2. Growth mechanism of self-assembled perovskite-spinel nanocomposites

Since the first report on the successful preparation of self-assembled nanocomposites via PLD in 2004, [15] considerable efforts have been made to gain a better understanding of the growth mechanism in order to further engineer the microstructure and properties. The self-assembled nanocomposites are commonly grown in a bottom-up process by PLD deposition in which the two phases nucleate separately on the substrate. As they grow, arriving flux diffuses on the surface and adds to each phase leading to a columnar two-phase structure.

The structural development is influenced by thermodynamic conditions such as the surface, interface and elastic strain energies of the two immiscible phases on a certain substrate. Considering the growth of a crystalline material on a substrate, the surface energies of the substrate, crystalline phase and the interface energy between them are γ_s, γ_c and γ_i. The formation of a film on the substrate leads to a surface energy change of $\Delta\gamma = \gamma_c + \gamma_i - \gamma_s$. If $\Delta\gamma < 0$, the crystalline phase is expected to fully wet the substrate and thus grow in the layer-by-layer mode, while if $\Delta\gamma > 0$, a lack of wetting of the crystalline phase on the substrate will promote the formation and growth of islands. [13-14, 16] The energy depends on the orientation of the surface and interface, therefore the epitaxial orientation plays an important role in determining the phase distribution and the morphology of the nanocomposites. Generally, the {001}

planes in the perovskite (BFO, BTO, etc.) and the {111} planes in the spinel (CFO, NFO, etc.) are the ones with lowest specific surface energy. [101-107]

Consider for example the well-studied BFO-CFO nanocomposites with a volume fraction of 1:1 reported by Zheng *et al*. [101] When epitaxially grown on an (001)-oriented STO substrate (700 °C, 100 mTorr oxygen), the (001)-oriented BFO phase can completely wet the substrate, but the (001)-oriented CFO does not wet the STO as a result of the higher surface energy and large lattice mismatch. This promotes the CFO phase to form nanopillars with a rectangular shape embedded in the coherent BFO matrix. TEM characterization suggests that the width of CFO pillars initially increases at the early stage of growth, and then remains unchanged if the growth conditions are stable, forming pillars with facetted tops which protrude above the BFO matrix. The CFO pillars exhibit characteristic {111}-type facets at the substrate interface and at the top surface, terminated by (001) (**Figure 2 (a)**). When grown on (111)-oriented STO (650 °C, 100 mTorr oxygen) the matrix and pillar phases are reversed. The {111} planes of CFO are parallel to the substrate surface, which promotes wetting of the substrate by the CFO. BFO pillars are embedded in the CFO matrix with a pyramidal shape with characteristic {001} facets at both substrate interface and surface (**Figure 2 (b)**). When grown on a (110)-oriented STO substrate (700 °C, 100 mTorr oxygen), a maze pattern of BFO and CFO is obtained. Cross section TEM further reveals that both BFO and CFO phases exhibit a columnar shape, suggesting similar initial wetting conditions (**Figure 2 (c)**).

During the growth of nanocomposites, the area of the vertical interfaces increases and the interface energy and strain become increasingly important. Comparing BFO-CFO with BTO-CFO nanocomposites (750–950 °C, 100 mTorr oxygen), the CFO pillars exhibit a highly faceted shape (rectangular or pyramidal) in BFO-CFO, but are cylindrical with a smaller diameter in BTO-CFO, as shown in **Figure 2 (d)**. [102] This has been attributed to the difference in the lattice mismatch. Specifically, the BFO (c≈3.965 Å) has a larger lattice mismatch with CFO (c/2≈4.20 Å) than with BTO (c≈4.05 Å). Therefore, a highly faceted morphology is preferred for CFO in the BFO matrix in order to minimize the elastic strain energy caused by the large lattice mismatch, while the cylindrical morphology of CFO in the BTO matrix minimizes surface energy per unit volume. [16] When the volume fractions of the two phases are dissimilar, the majority phase can form the matrix irrespective of the epitaxial orientation. However, the orientation significantly affects the morphology of the pillars. Wang *et al.* observed that the CFO phase exhibits rectangular pillars in (001)-oriented BFO-rich nanocomposites (700 °C, 150 mTorr oxygen), similar to that in composites with a BFO-CFO ratio of 1:1 (**Figure 3 (a)**). [103] In (111)-oriented BFO-rich nanocomposites, the CFO forms triangular prisms embedded in the

BFO matrix, while in (110)-oriented BFO-rich nanocomposites grown at the same conditions, the CFO phase forms fin-like structures with the long axis along the in-plane [$\bar{1}$10] direction, as shown in **Figure 3 (b)** and **(c)**.

The results discussed above correspond to nanocomposites grown on STO (a = 3.905 Å), in which both perovskite and spinel have the same crystallographic orientation with the substrate. Liao *et al.* observed that the orientations of BFO and CFO can be different by growing the nanocomposites on various substrates (700 °C, 200 mTorr oxygen). [104] They compared two other perovskite substrates, i.e. $(001)_{pc}$-oriented $DyScO_3$ (DSO, with a pseudocubic (pc) lattice constant of 3.94 Å) and $NdGaO_3$ (NGO, with a pseudocubic lattice constant of 3.85 Å). The BFO matrix was (001)-orientated in all cases, but the CFO phase was (110)-oriented for the nanocomposite on DSO, and (111)-oriented for that on NGO. The morphology of the CFO phases reflects their crystallographic orientation, forming fin-like nanobelts on $(001)_{pc}$-oriented DSO and triangular islands on $(001)_{pc}$-oriented NGO unlike the rectangular pillars on (001)-oriented STO, as shown in **Figure 3 (d)-(f)**. This illustrates a role of lattice mismatch between CFO and the substrate on the morphology.

The substrate strain not only affects the CFO phase, but also influences the crystal structure of BFO. When grown on a substrate with larger compressive strain (>4.5%), e.g. $LaAlO_3$ (LAO, with a pseudocubic lattice constant of 3.79 Å), the BFO can exhibit a T-like structure with lattice constants of 3.67 Å in-plane and 4.65 Å out-of-plane. T-like BFO can also form nanocomposites with CFO. [105] In the BFO-rich nanocomposites grown on (001)-oriented LAO substrate, the matrix phase is indeed the T-like BFO, but the crystallographic orientation and morphology of the CFO differs from that of nanocomposites comprising R-like BFO. Amrillah *et al.* prepared T-like BFO-CFO nanocomposites at 650 °C, 100 mTorr oxygen with a volume ratio of BFO:CFO = 4:1 on $(001)_{pc}$-oriented LAO, and observed triangular (111)-oriented CFO islands. [106] However, in T-like BFO-CFO nanocomposites grown at 625 °C with a ratio of 2:1 on $(001)_{pc}$ -oriented LAO substrate, the CFO forms rectangular (001)-oriented pillars. [107] The out-of-plane lattice parameters of T-like BFO and CFO are 4.625 Å and 8.391 Å, and semi-coherent interfaces between T-like BFO and CFO are observed due to the large lattice mismatch.

Zheng *et al.* systematically studied the impact of kinetic factors on the CFO pillars in both BFO-CFO and BTO-CFO by modeling the growth of nanocomposites as a 2-D diffusion process in which the transport is limited to the solid-vapor interface, and predicted, in agreement with the experimental observations, that attributes of the nanopillars can be controlled by the growth temperature and rate. [101] Specifically, the dimensions of pillars increase with an increase in substrate temperature and a decrease in

growth rate. However, high temperatures (> 675 °C) can cause the decomposition of BFO due to loss of the highly volatile Bi [108] and the growth must be carried out in regimes of temperature, pressure and gas ambient that lead to formation of both phases on the nanocomposites.

3.3. Tuning the ferroelectric and magnetic properties of self-assembled nanocomposites

There are several strategies for manipulating the ferroic properties of the perovskite and spinel constituents of nanocomposites. For BFO, the ferroelectric performance of single-phase films has been engineered by varying the growth conditions, [86] utilizing vicinal substrates, [87] and tuning the buffer thickness. [109]. In addition, the discovery of the T-like phase opens up new directions to tune the ferroelectric properties since the morphotropic phase boundary between R-like and T-like BFO can significantly enhance the electromechanical response. This has stimulated research on nanocomposites with T-like or mixed-phase BFO as the matrix. T-like BFO is promoted by growth on LAO, and its larger out-of-plane lattice parameter of ~4.65 Å leads to out-of-plane tensile strain in the CFO pillars [107].

The magnetic anisotropy and other magnetic properties of the spinel phase have been studied extensively, and depend on crystallographic orientation, shape and strain state of the spinel. In BFO-CFO or BTO-CFO nanocomposites grown on (001)-oriented STO, an out-of-plane easy magnetic axis is typically present. [103, 110] The elongated shape of the pillars leads to shape anisotropy which decreases as the aspect ratio (film thickness divided by the lateral size of the CFO pillars) decreases. [103] The magnetoelastic anisotropy is a significant source of anisotropy and may even be the dominant contribution. For example, removing the BFO matrix by chemical etching leads to a relaxation in strain in the CFO pillars and a reduction in anisotropy. [111] Lattice mismatch with the substrate also causes strain in the CFO for low aspect ratio pillars. The total anisotropy also includes the magnetocrystalline anisotropy, which favors magnetization along the <001> directions of CFO.

The morphology of the CFO phase plays an important role in the magnetic properties. On (110)-oriented STO substrates, fin-like CFO crystals are embedded in the BFO matrix with the long side along the in-plane $[\bar{1}10]$ direction, the short side along the in-plane [001] direction, [103] and the easy axis along $[\bar{1}10]$. For BFO-CFO grown on (111)-oriented STO where the CFO forms triangular prisms, an in-plane easy axis was observed despite the out-of-plane compressive strain. [103] Changing the substrate can vary the crystallographic orientation and shape of the CFO phase. For example in BFO-CFO on $(001)_{pc}$-oriented DSO the CFO formed (110)-oriented fins with their long axis and magnetic easy axis

along the in-plane [$\bar{1}$10] direction. [104] Kim *et al.* showed that CFO pillars had much larger dimensions and spacing when grown on (001)-oriented STO coated with a buffer layer of $SrTi_{0.78}Cu_{0.22}O_{3-\delta}$ (STCu). The STCu itself formed a three-phase epitaxial nanocomposite consisting of a perovskite matrix with vertical core-shell metal (Cu)-rock salt (SrO) nanorods. [112] **Figure 4 (a)** shows the STCu nanocomposite and **Figure 4 (b)** shows that the Cu can be etched to leave nanopores. The subsequent growth of BFO-CFO nanocomposites on the STCu yielded CFO pillars with a much larger characteristic dimension and a lower magnetic anisotropy and coercivity compared to a nanocomposite grown directly onto (001)-oriented STO (**Figure 4 (c)-(f)**), suggesting faster surface diffusion or lower pillar nucleation density. In another example, Kim *et al.* demonstrated the effect of changing temperature during the deposition. [66] By lowering the temperature from 650 °C to 560 °C, the pillar diameter decreased and the final shape resembled a bowling pin. Compared with the single-step grown nanocomposites (650 °C), the heteromorphic CFO showed a lower anisotropy, coercivity and saturation field. CFO can be grown as the matrix phase in BFO-CFO nanocomposites on (111)-oriented STO, exhibiting an in-plane easy axis dominated by shape [113-114].

Engineering the strain state of the CFO to tune the magnetic properties mainly relies on the modification of the perovskite matrix, for example, a change from R-like to T-like BFO. In the R-like BFO-CFO nanocomposites (for instance grown on STO), the CFO pillars undergo an out-of-plane compressive strain which promotes perpendicular magnetic anisotropy. However, in the T-like BFO-CFO nanocomposite (grown on LAO), the T-like BFO matrix with its out-of-plane lattice parameter of c = 4.65 Å produces a tensile strain in the CFO (c/2=4.20 Å), promoting an in-plane easy axis as observed by Dix *et al.,* **Figure 5 (a)** and **(b)**. [107] In other examples, a BTO matrix leads to out-of-plane compressive strain in the CFO [15], while $PbTiO_3$ leads to an out-of-plane tensile strain in the CFO. [115]

Different spinel compositions have been incorporated into nanocomposites, including NFO and MFO. NFO has a smaller magnetostriction than CFO and a smaller strain due to the lower lattice mismatch with BFO, whereas MFO has a negligible magnetostriction and small magnetization. Kim *et al.* demonstrated nanocomposites made by changing between CFO and MFO compositions during growth. [17] Cation interdiffusion between CFO and MFO was observed, but this was suppressed using blocking layers of BFO to form BFO–(CFO/BFO/MFO) nanocomposites. The morphology, pillar composition and magnetic hysteresis depend on the thickness of the blocking layer, and two-step switching was observed if the CFO and MFO pillars were magnetically decoupled. Changing the ratio of CFO to MFO enabled control over the saturation magnetization and the coercivity (**Figure 5 (c)-(h)**).

4. Sputtered multiferroic nanocomposites for scalable fabrication

4.1. Sputter-grown oxide films and nanocomposites

Vertical epitaxial nanocomposites are commonly grown by PLD on single crystal oxide substrates which limits their utility in microelectronic devices. While PLD is an attractive growth method for research purposes, it falls short in terms of uniformity over substrate areas larger than ~1 cm. Sputtering is preferred for larger scale production, in which the sputtered film is formed from atoms ejected from a solid target material via momentum exchange from bombardment by energetic ions such as Ar^+ generated in a glow discharge plasma [116]. Radio frequency (RF) glow discharges [117] enable growth of insulating thin films, and sputtering yields are greatly enhanced by using a magnetron which confines the charged particles close to the target. [118]

Advances in sputter deposition techniques have led to the growth of high quality complex oxide thin films of high temperature superconductors, [119-120] ferroelectrics, [121-122] metal-insulator transition materials, [123-124] conductive electrodes, [125-126] and energy devices, [127-128] as well as epitaxial or superlattice [129-130] structured oxide thin films. There has been extensive work on sputtered BTO [131-133] and BFO. [132, 134] Epitaxial BFO thin films were grown on miscut (001), (101), and (111)-oriented STO substrates using high rate off-axis sputtering, [122, 135] with ferroelectric loops shown in **Figure 6 (a)** and **(b)**. Substrate miscut raised the remnant polarization P_r and enabled selection of certain domain variants which affect the ferroelectric switching behavior and leakage current. Sputtered CFO has also been reported [136-138], illustrating for example the effect of thickness, strain and oxygen flow rate on magnetic hysteresis.

Sputtering has also been used for epitaxial growth of 2-2 type spinel/perovskite bilayer nanocomposite thin films to realize a magnetoelectric heterostructure. Wang et al. fabricated a bilayer thin film consisting of BFO (220 nm)/CFO (180 nm) on SRO-buffered $Pt/TiO_2/SiO_2/Si$ which exhibited a P_r of ~146 $\mu C/cm^2$ and a coercive field of ~ 1803 kV/cm, together with a saturation magnetization of 140 emu/cm^3 and a coercive field of ~2.7 kOe as shown in **Figure 6 (c)** and **(d)**. [139] While the bilayer nanocomposites showed potential for a multiferroic device application, the leakage current was excessive. Lowering the CFO thickness reduced the leakage current as well as the saturation magnetization and coercive field (**Figure 6 (e, f)**). [140]

Despite the extensive work on sputtered epitaxial oxides or bilayers of perovskites and spinels, there is very little work on the fabrication of vertically aligned perovskite-spinel epitaxial nanocomposites using sputtering. The structure, dielectric properties, and magnetocapacitance of BTO-CFO

nanocomposites grown using sputtering has been reported. [141-144] Yang *et al.* discussed self-assembled growth, dielectric property, and leakage current of sputtered BTO-CFO nanocomposites. Compared with a single BTO layer, the nanocomposites showed higher dielectric constants and lower dielectric loss, and properties were engineered by adjusting deposition conditions. [145]

Kim *et al.* reported the sputter growth of BFO-CFO VANs on Nb:STO substrates for the first time. [146] Deposition at 650 °C in an oxygen and argon plasma yielded a columnar epitaxial structure in which BFO and CFO grew with a cube-on-cube epitaxy on Nb:STO substrates, as seen in PLD films. The BFO and CFO were highly strained along the out-of-plane direction but this was relaxed on annealing. However, sputtered nanocomposites also exhibited rectangular CFO pillars oriented along the <110> directions of the substrate as shown in **Figure 7 (a)**, and the BFO consisted of a minority of T-like BFO and majority of R-like BFO at certain growth conditions, **Figure 7 (b),** unlike nanocomposites grown on STO or Nb:STO using PLD. The sputtered nanocomposites exhibited both magnetic and ferroelectric signals as shown in **Figure 7 (c) and (d)**, which were similar to those of nanocomposites with only R-like BFO. Sputter-grown nanocomposites revealed an out-of-plane magnetic easy axis as a result of both shape and a dominant magnetoelastic anisotropy, and the effects of strain were confirmed by removing the BFO phase with chemical etching, **Figure 7 (e)-(g).**

The deposition conditions affect the structure and magnetic properties of sputtered BFO-CFO nanocomposites. [147] The surface morphology of nanocomposites grown at a lower working pressure or higher RF power were rougher, and the CFO particles were rounded, while higher working pressures or lower RF power promoted a well-defined VAN with a strong out-of-plane magnetic anisotropy. Films grown with little or no oxygen in the plasma were also rough and magnetically isotropic (**Figure 8 (a)-(b) and (d)-(e)**) while oxygen improved the surface morphology and raised the out-of-plane magnetic anisotropy as shown in **Figure 8 (c) and (f)**. The effect of deposition conditions is shown in **Figure 8 (g)**.

A conductive bottom electrode layer is essential for electrically characterizing nanocomposites grown on STO and other insulating substrates. Lee *et al.* reported the growth of sputtered BFO-CFO nanocomposites on annealed $La_{0.7}Sr_{0.3}MnO_3$ (LSMO) layers and concluded that the magnetic anisotropy can be tuned via the LSMO thickness. [148] Nanocomposites on 20 and 50 nm thick LSMO shown in **Figure 9 (a)** and **(b)** exhibited almost identical morphologies, but the magnetic anisotropy changed from out-of-plane to in-plane easy axis on increasing the LSMO thickness as a result of strain relaxation of CFO, **Figure 9 (c)** and **(d)**. The polarization could be reversed, **Figure 9 (e)**, and ferroelectric response was evident from the hysteresis data, **Figure 9 (f)**.

4.2. Integration of epitaxial perovskite-spinel nanocomposites on Si substrates

Integration of epitaxial oxides with Si constitutes a route for bringing the functionality of various oxides to technologically mature, scalable semiconductor technology. [149-153] However, direct integration of epitaxial complex oxides onto Si substrates has been challenging due to the easily formed amorphous SiO_2 layer on Si surface, which impedes epitaxial growth. Various buffer layers on Si have been used to fabricate epitaxial perovskite or spinel oxide thin films. For perovskites such as $(La,Sr)CoO_3$, $BiFeO_3$, $Pb(Zr,Ti)O_3$, and $LaNiO_3$, a buffer layer consisting of a bilayer of CeO_2 on yttrium-stabilized zirconia (YSZ) has been used. [154-157] However, CFO grew with (111) out-of-plane orientation on CeO_2/YSZ-buffered Si (001) [158], and a trilayer buffer consisting of perovskite/CeO_2/YSZ-buffered Si (001) was therefore selected for growth of both spinel and perovskite phases. An alternative to using multilayer buffer layers is to grow an STO layer directly on Si. The Si has a lattice parameter of a = 5.431 Å, and bulk STO (3.905 Å) has a reasonable lattice match to Si $a/\sqrt{2}$ = 3.840 Å. STO/Si (001) has been grown by oxide MBE, [159-161] in which STO, of order 8 nm thickness, was formed by a multistep procedure of substrate cleaning in a strong oxidant (H_2SO_4:H_2O_2) at 130 °C for 10 mins, followed by removal of the native oxide using HF:H_2O for 30 s, then oxide growth, desorption and deposition of STO at 600 °C.

Sawamura *et al.* reported the structure and modification of magnetic and ferroelectric properties of BTO-CFO vertical nanocomposites on trilayer buffer layers consisting of $(La,Sr)CoO_3$/CeO_2/YSZ. [162] Kim *et al.* grew BFO-CFO nanocomposites by PLD on a trilayer buffer of $Sr(Ti_{0.65}Fe_{0.35})O_3$ (STF35)/CeO_2/YSZ on Si which showed the same morphology as those grown directly on STO (001) (**Figure 10 (a) and (b)**), while CFO pillars grew with 45° rotation on buffered Si with rough STF35 (**Figure 10 (c)**). [65] The roughness was believed to provide more nucleation sites for CFO. BFO-CFO nanocomposites were also integrated on STO-buffered silicon as shown in **Figure 10 (d)**. The nanocomposites showed a much higher out-of-plane compressive strain and magnetic anisotropy compared to those grown on STO, and an anisotropy field of about 23 kOe. [146] As in the case of PLD films, the sputtered nanocomposites on STO/Si showed a similar structure but higher magnetic anisotropy compared to sputtered nanocomposites on STO and Nb:STO (**Figure 10 (e) and (f)**). Nanocomposites were also sputtered onto 20 nm thick LSMO/8 nm thick STO/Si substrates. [148] The BFO-CFO nanocomposite on LSMO/STO/Si substrates showed similar structure and ferroelectric properties but a higher magnetic anisotropy compared to nanocomposites on single crystal Nb:STO or on 20 nm LSMO/STO. These results show that sputter deposition is a viable method for growing nanocomposites on buffered Si.

4.3. Templated self-assembly of perovskite-spinel nanocomposites

In order to apply the 1-3 type multiferroic BFO-CFO nanocomposite thin film for a memory device, it is preferable that the ferromagnetic pillars are regularly arranged within the ferroelectric matrix, which requires templating of their nucleation sites. Come*s et al.* presented a technique to produce ordered square arrays of CFO pillars on a Nb:STO substrate by patterning a thin CFO layer into seed particles using electron-beam lithography, followed by growth of BFO. [26] **Figure 11** illustrates the templating process and properties of the ordered BFO-CFO nanocomposite, which was grown using pulsed electron deposition. If the spacing of nucleation sites exceeds the diffusion distance of the CFO, additional pillars form, as seen for 200 nm spaced templates. The magnetic anisotropy was low and the CFO was magnetized in plane.

Stratulat *et al.* grew templated BFO-CFO nanocomposites on SRO buffered STO (001) substrates via PLD. [25] The nucleation sites were made by depositing CFO through an AAO template, creating a close packed array of CFO seeds, **Figure 12 (a)**. Square and rectangular pyramidal CFO pillars in the BFO matrix are shown in **Figure 12 (b)**, along with the ferroelectric and magnetic response. The patterned nanocomposite showed a typical butterfly ferroelectric hysteresis loop with piezoelectric coefficient of ~30 pm/V. The estimated ME coupling via magnetocapacitance measurement was ~ 0.9 μC/cm·Oe. AAO templates have been used to form highly-ordered arrays of ferroelectric/ferromagnetic bilayer nanodots, a 0-0 type heterostructure, on STO or Nb:STO substrates using PLD. [163-165] In particular, Tian *et al.* reported epitaxial BFO/CFO heterostructured nanodots on SRO-coated STO substrates grown using PLD as illustrated in **Figure 12 (c-e)**. [165] The nanodots exhibited an average lateral size of ~70 nm with 110 nm spacing, and showed a low magnetic anisotropy and an in-plane easy axis. There is an enhancement of piezoelectric effects due to the reduced substrate clamping effect compared to that of bilayer epitaxial nanocomposite thin films. The lateral ME coefficient, measured by comparing piezoresponse loops at zero and 3000 Oe magnetic field, was 1.2×10^4 mV/cm·Oe, which was two orders larger than that of 0-3 type nanocomposites [35] and comparable to those of PZT/CFO core-shell nanofiber structures [166]. A reverse ME effect was also observed in which electric field affects the magnetization, **Figure 12 (e)**.

Choi *et al.* formed ordered BFO-CFO nanocomposite films with a square symmetry by using a self-assembled triblock terpolymer as an etch mask to pattern nucleation sites into a Nb:STO substrate then growing the nanocomposite using PLD. [28] The experimental process and templated

nanocomposites are illustrated in **Figure 13 (a, b)**. Even though the long range order is poorer than that of direct-write processes, the polymer provided a much smaller periodicity of 44 nm.

Aimon *et al.* reported the growth of square arrays of CFO nanopillars in a BFO matrix using selective nucleation in pits formed in Nb:STO using a Ga focused ion beam (FIB) as summarized in **Figure 13 (c)**. [27] Ordered arrays of 2 nm to 8.5 nm deep pits and trenches were formed at the ion-damaged regions by selectively etching in an aqueous acid solution. A thin CFO film was deposited at a low deposition rate to guarantee a high surface diffusion and then a 4 nm thick BFO film was grown, which covered the remaining areas of the substrate. The resulting thin, well-ordered BFO-CFO composite layer was then used as a guide for the directed growth of a thick nanocomposite. A variety of template patterns makes various ordered arrays with different orientations and periods in the 60–100 nm range, **Figure 13 (d)**. This templating method was used to grow BFO-$Co_xNi_{1-x}Fe_2O_4$ with excellent order [75] and BFO-MFO with an array of parallel trenches along the <110> direction as shown in **Figure 13 (d)**. The CFO pillars exhibited single-domain magnetic contrast and ferroelectric domains were clearly visible in the BFO matrix. [167] The CFO pillars switched upon applying an electric field to the BFO matrix, indicating magnetoelectric coupling. Kim *et al*. extended this templating method to successfully fabricate ordered BFO-CFO nanocomposites on a template using sputtering instead of PLD, extending the potential utility of ME nanocomposites in devices. [146]

5. Conclusions and outlook

Magnetoelectric multiferroics which show simultaneous ferroelectric and ferri-/ferromagnetic ordering with strong magnetoelectric coupling exhibit unusual and exciting phenomena. Single phase multiferroics are rare and their magnetoelectric couplings are relatively weak at room temperature which limits their practical applications. In contrast, multiferroic composites combining both ferroelectric and ferri-/ferromagnetic phases coupled by strain yield higher magnetoelectric coupling response above room temperature which are very promising for application as a high density device. Three types of multiferroic nanocomposites, 0-3, 2-2 and 1-3 types, were introduced in this review with a focus on the 1-3 type nanocomposite thin films consisting of vertically aligned spinel pillars in a perovskite matrix.

We reviewed recent progress in the growth, characterization and understanding of vertically aligned BFO-CFO nanocomposites. Both phases grow epitaxially on the substrate and strain is transferred between the spinel and perovskite at the vertical interface. The interface strain plays an important role in coupling the magnetic and ferroelectric properties via the magnetostriction and piezoelectric response of the two phases. Nanocomposites have been commonly grown using PLD on single crystal oxide

substrates, but recent work has demonstrated sputter deposition of nanocomposites, as well as growth on Si via a buffer layer, and templating of the locations of the magnetic pillars. This facilitates the integration of multiferroic nanocomposites in device manufacturing by providing a large area deposition method for growth on Si. Several magnetoelectric device concepts were reviewed, and new multiferroic memory devices that could take advantage of highly ordered magnetic nanopillars in a ferroelectric matrix on Si substrates may now be possible. It is challenging to grow epitaxial nanocomposites directly on a Si substrate, but buffer layers can provide a platform for epitaxial growth. Furthermore, buffer layers could provide an innovative way to grow epitaxial nanocomposites on sacrificial layers such as $Sr_3Al_2O_6$ [168-169], NaCl [170-171], and graphene [172], which can be completely removed by etching. This could provide a fabrication process to lay out metallic bottom electrode lines which would otherwise interrupt the epitaxial growth of oxide nanocomposites at high temperature. In the future, continuing improvements in materials growth and properties, and particularly in the magnetoelectric coupling, will enable these nanocomposites to be used in high density logic and memory devices.

Conflicts of interest

There are no conflicts to declare.

Acknowledgments

This work was supported by the Basic Science Research Program through the National Research Foundation of Korea (NRF) funded by the Ministry of Science, ICT & Future Planning (NRF-2018R1D1A1B07043325). This work is supported in part by the National Science Foundation DMR1419807 and by SMART, an nCORE Center of the Semiconductor Research Corporation program sponsored by the National Institute of Standards and Technology.

References

1. J. F. Scott, *Annu. Rev. Mater. Sci.*, 1998, **28**, 79.

2. R. Bez, E. Camerlenghi, A. Modelli and A. Visconti, *Proc. IEEE*, 2003, **91**, 489.

3. M. Wuttig, *Nat. Mater.*, 2005, **4**, 265.

4. M. H. R. Lankhorst, B. W. S. M. M. Ketelaars and R. A. M. Wolters, *Nat. Mater.,* 2005, **4**, 347.

5. D.-H. Kwon, K. M. Kim, J. H. Jang, J. M. Jeon, M. H. Lee, G. H. Kim, X.-S. Li, G.-S. Park, B. Lee, S. Han, M. Kim and C. S. Hwang, *Nat. Nanotech.*, 2010, **5**, 148.

6. J. F. Scott and C. A. P. de Araujo, *Science*, 1989, **246,** 1400.

7. Y. Arimoto and H. Ishiwara, *MRS Bull.*, 2004, **29**, 823

8. J. Åkerman, *Science*, 2005, **308,** 508.

9. W. J. Gallagher and S. S. P. Parkin, *IBM J. Res. Dev.*, 2006, **50**, 5.

10. J. F. Scott, *Nat. Mater.,* 2007, **6**, 256.

11. L. W. Martin, Y.-H. Chu and R. Ramesh, *Emerging Non-Volatile Memories*, Springer, New York City, 2014.

12. D. Khomskii, *Physics*, 2009, **2**, 20.

13. J. L. MacManus-Driscoll, P. Zerrer, H. Wang, H. Yang, J. Yoon, A. Fouchet, R. Yu, M. G. Blamire and Q. Jia, *Nat. Mater.,* 2008, **7**, 314.

14. A. Chen, Z. Bi, Q. Jia, J. L. MacManus-Driscoll and H. Wang, *Acta Mater.*, 2013, **61**, 2783.

15. H. Zheng, J. Wang, S. E. Lofland, Z. Ma, L. Mohaddes-Ardabili, T. Zhao, L. Salamanca-Riba, S. R. Shinda, S. B. Ogale, F. Bai, D. Viehland, Y. Jia, D. G. Schlom, M. Wuttig, A. Roytburd and R. Ramesh, *Science*, 2004, **303**, 661.

16. J. L. MacManus-Driscoll, *Adv. Funct. Mater.,* 2010, **20**, 2035.

17. D. H. Kim, N. M. Aimon, X. Y. Sun and C. A. Ross, *Adv. Funct. Mater.,* 2014, **24**, 2334.

18. R. M. Bozorth, E. F. Tilden and A. J. Williams, *Phys. Rev.,* 1955, **99**, 1788.

19. J. Wang, J. B. Neaton, H. Zheng, V. Nagarajan, S. B. Ogale, B. Liu, D. Viehland, V. Vaithyanthan, D. G. Scholm, U. V. Waghmare, N. A. Spaldin, K. M. Rabe, M. Wuttig and R. Ramesh, *Science,* 2003, **299**, 1719.

20. C.-W. Nan, G. Liu, Y. Lin and H. Chen, *Phys. Rev. Lett.*, 2005, **94**, 197203.

21. M. Rafique, A. Herklotz, E.-J. Guo, R. Roth, L. Schultz, K. Dörr and S. Manzoor, J. Appl. Phys., 2013, **114**, 233910.

22. M. Rafique, A. Herklotz, K. Dörr and S. Manzoor, *Appl. Phys. Lett.*, 2017, **110**, 202902.

23. Z. Wang, Y. Yang, R. Viswan, J. Li and D. Viehland, *Appl. Phys. Lett.*, 2011, **99**, 043110.

24. F. Zavaliche, H. Zheng, L. Mohaddes-Ardabili, S. Yang, Q. Zhan, P. Shafer, E. Reilly, R. Chopdekar, Y. Jia and P. Wright, *Nano Lett.*, 2005, **5**, 1793.

25. S. M. Stratulat, X. Lu, A. Morelli, D. Hesse, W. Erfurth and M. Alexe, *Nano Lett.*, 2013, **13**, 3884.

26. R. Comes, H. Liu, M. Khokhlov, R. Kasica, J. Li and S. A. Wolf, *Nano Lett.*, 2012, **12**, 2367.

27. N. M. Aimon, H. K. Choi, X. Y. Sun, D. H. Kim and C. A. Ross, *Adv. Mater.*, 2014, **26**, 3063.

28. H. K. Choi, N. M. Aimon, D. H. Kim, X. Y. Sun, J. Gwyther, I. Manners and C. A. Ross, *ACS Nano*, 2014, **8**, 9248.

29. J. Zhai, N. Cai, Z. Shi, Y. Lin and C.-W. Nan, *J. Phys. D*, 2004, **37**, 823.

30. J. G. Wan, X. W. Wang, Y. J. Wu, M. Zeng, Y. Wang, H. Jiang, W. Q. Zhou, G. H. Wang and J.-M. Liu, *Appl. Phys. Lett.*, 2005, **86**, 122501.

31. H. Ryu, P. Murugavel, J. H. Lee, S. C. Chae, T. W. Noh, Y. S. Oh, H. J. Kim, K. H. Kim, J. H. Jang, M. Kim, C. Bae and J. G. Park, *Appl. Phys. Lett.*, 2006, **89**, 102907.

32. X. L. Zhong, J. B. Wang, M. Liao, G. J. Huang, S. H. Xie, Y. C. Zhou, Y. Qiao and J. P. He, *Appl. Phys. Lett.*, 2007, **90**, 152903.

33. A. McDannald, M. Staruch, G. Sreenivasulu, C. Cantoni, G. Srinivasan and M. Jain, *Appl. Phys. Lett.*, 2013, **102**,122905.

34. Y. Li, Z. Wang, J. Yao, T. Yang, Z. Wang, J.-M. Hu, C. Chen, R. Sun, Z. Tian, J. Li, L.-Q. Chen and D. Viehland, *Nat. Commun.*, 2015, **6**, 6680.

35. T. Wu, M. A. Zurbuchen, S. Saha, R.-V. Wang, S. K. Streiffer and J. F. Mitchell, *Phys. Rev. B*, 2006, **73**, 134416.

36. W. Eerenstein, M. Wiora, J. L. Prieto, J. F. Scott and N. D. Mathur, *Nat. Mater.*, 2007, **6**, 348.

37. C. Thiele, K. Dörr, O. Bilani, J. Rödel and L. Schultz, *Phys. Rev. B*, 2007, **75**, 054408.

38. J. Wang, Y. Zhang, J. Ma, Y. Lin and C.-W. Nan, *J. Appl. Phys.*, 2008, **104**, 014101.

39. S. Ryu, J. H. Park and H. M. Jang, *Appl. Phys. Lett.*, 2007, **91**, 142910.

40. M. Ziese, A. Bollero, I. Panagiotopoulos and N. Moutis, *Appl. Phys. Lett.*, 2006, **88**, 212502.

41. Y. G. Ma, W. N. Cheng, M. Ning and C. K. Ong, *Appl. Phys. Lett.*, 2007, **90**, 152911.

42. N. Ortega, P. Bhattacharya, R. S. Katiyar, P. Dutta, A. Manivannan, M. S. Seehra, I. Takeuchi and S. B. Majumder, *J. Appl. Phys.*, 2006, **100**,126105.

43. Y. Zhang, C. Deng, J. Ma, Y. Lin and C.-W. Nan, *Appl. Phys. Lett.*, 2008, **92**, 062911.

44. H. C. He, J. Ma, Y. H. Lin and C. W. Nan, *J. Phys. D: Appl. Phys.*, 2009, **42**, 095008.

45. M. Feng, J. Wang, J. Hu, J. Wang, J. Ma, H. Li, Y. Shen, Y. Lin, L. Q. Chen and C. W. Nan, *Appl. Phys. Lett.*, 2015, **106**, 072901.

46. J. A. Mundy, C. M. Brooks, M. E. Holtz, J. A. Moyer, H. Das, A. F. Rébola, J. T. Heron, J. D. Clarkson, S. M. Disseler, Z. Liu, A. Farhan, R. Held, R. Hovden, E. Padgett, Q. Mao, H. Paik, R. Misra, L. F. Kourkoutis, E. Arenholz, A. Scholl, J. A. Borchers, W. D. Ratcliff, R. Ramesh, C. J. Fennie1, P. Schiffer, D. A. Muller and D. G. Schlom, *Nature*, 2016, **537**, 523.

47. G. Liu, C.-W. Nan, Z. K. Xu and H. Chen, *J. Phys. D: Appl. Phys.*, 2005, **38**, 2321.

48. K. S. Kim, S. H. Han, H. G. Kim, J. S. Kim and C. I. Cheon, *J. Vac. Sci. Technol. B*, 2010, **28**, C5A14.

49. F. Bai, H. Zhang, J. Li and D. Viehland, *J. Phys. D: Appl. Phys.*, 2010, **43**, 285002.

50. C. Schmitz-Antoniak, D. Schmitz, P. Borisov, F. M. F. de Groot, S. Stienen, A. Warland, B. Krumme, R. Feyerherm, E. Dudzik, W. Kleemann and H. Wende, *Nat. Commun.*, 2013, **4**, 2051.

51. F. Zavaliche, T. Zhao, H. Zheng, F. Straub, M. P. Cruz, P. L. Yang, D. Hao and R. Ramesh, *Nano Lett.*, 2007, **7**, 1586.

52. L. Yan, Z. P. Xing, Z. G. Wang, T. Wang, G. Y. Lei, J. F. Li and D. Viehland, *Appl. Phys. Lett.*, 2009, **94**, 192902.

53. Y. S. Oh, S. Crane, H. Zheng, Y. H. Chu, R. Ramesh and K. H. Kim, *Appl. Phys. Lett.*, 2010, **97**, 052902.

54. J. Li, I. Levin, J. Slutsker, V. Provenzano, P. K. Schenck, R. Ramesh, J. Ouyang and L. Roytburd, *Appl. Phys. Lett.*, 2005, **87**, 072909.

55. J. G. Wan, Y. Y. Weng, Y. J. Wu, Z. Y. Li, J. M. M. Liu and G. H. Wang, *Nanotechnology*, 2007, **18**, 465708.

56. Z. Tan, J. Slutsker and A. L. Roytburd, *J. Appl. Phys.*, 2009, **105**, 061615.

57. L.-Y. Ding, F.-X. Wu, Y.-B. Chen, Z.-B. Gu and S.-T. Zhang, *Appl. Surf. Sci.*, 2011, **257**, 3840.

58. D. H. Kim, N. M. Aimon and C. A. Ross, *J. Appl. Phys.*, 2013, **113**, 17B510.

59. Q. Zhan, R. Yu, S. P. Crane, H. Zheng, C. Kisielowski and R. Ramesh, *Appl. Phys. Lett.*, 2005, **89**, 172902.

60. D. H. Kim, T. C. Kim, S. H. Lee, S. H. Han, K.-S. Han and C. A. Ross, *J. Appl. Phys.*, 2017, **121**, 163902.

61. J. van Suchtelen, *Phil. Res. Rep.*, 1972, **27**, 28.

62. J. Wang, *Multiferroic Materials: Properties, Techniques, and Applications*, CRC Press, Boca Raton, 2016.

63 K.-H. Hellwege, A. M. Hellwege, *Magnetic and Other Properties of Oxides and Related Compounds*, Springer, Berlin, 1970.

64. N. M. Aimon, D. H. Kim, H. K. Choi and C. A. Ross, *Appl. Phys. Lett.*, 2012, **100**, 092901.

65. D. H. Kim, N. M. Aimon, X. Sun, L. Kornblum, F. J. Walker, C. H. Ahn and C. A. Ross, *Adv. Func. Mater.,* 2014, **24**, 5889.

66. D. H. Kim, N. M. Aimon and C. A. Ross, *APL Mater.,* 2014, **2**, 081101.

67. R. Comes, M. Khokhlov, H. Liu, J. Lu and S. A. Wolf, *J. Appl. Phys.*, 2012, **111**, 07D914.

68. M. Gajek, M. Bibes, S. Fusil, K. Bouzehouane, J. Fontcuberta, A. Barthélémy and A. Fert, *Nat. Mater.*, 2007, **6**, 296.

69. Y. Zhang, Z. Li, C. Deng, J. Ma, Y. Lin and C.-W. Nan, *Appl. Phys. Lett.*, 2008, **92**, 152510.

70. M. Bibes and Agnès Barthélémy, *Nat. Mater.*, 2008, **7**, 425.

71. M. G. Mankalale, Z. Liang, Z. Zhao, C. H. Kim, J.-P. Wang and S. S. Sapatnekar, *IEEE J. Explor. Solid-State Computat. Devices Circuits*, 2017, **3**, 27.

72. S. Manipatruni, D. E. Nikonov, C.-C. Lin, T. A. Gosavi, H. Liu, B. Prasad, Y.-L. Huang, E. Bonturim, R. Ramesh and I. A. Young, *Science*, 2019, **565**, 35.

73. S. A. Wolf, J. Lu, M. R. Stan, E. Chen and D. M. Treger, *Proc. IEEE*, 2010, **98**, 2155.

74. A. Imre, G. Csaba, L. Ji, A. Orlov, G. H. Bernstein and W. Porod, *Science*, 2006, **311**, 205.

75. S. Ojha, W. C. Nunes, N. M. Aimon and C. A. Ross, *ACS Nano*, 2016, **10**, 7657.

76. D. B. Chrisey and G. K. Hubler, *Pulsed Laser Deposition of Thin Films*, John Wiley & Sons, New Jersey, 1994.

77. M. N. R. Ashfold, F. Claeyssens, G. M. Fuge and S. J. Henley, *Chem. Soc. Rev.*, 2004, **33**, 23.

78. J. Li, Wang, M. Wuttig, R. Ramesh, N. Wang, B. Ruette, A. P. Pyatakov, A. K. Zvezdin and D. Viehland, *Appl. Phys. Lett.*, 2004, **84**, 5261.

79. X. Qi, J. Dho, R. Tomov, M. G. Blamire and J. L. MacManus-Driscoll, *Appl. Phys. Lett.*, 2005, **86**, 062903.

80. J. B. Neaton, C. Ederer, U. V. Waghmare, N. A. Spaldin and K. M. Rabe, *Phys. Rev. B*, 2005, **71**, 014113.

81. D. Sando, B. Xu, L. Bellaiche and V. Nagarajan, *Appl. Phys. Rev.*, 2016, **3**, 011106.

82. D. Sando, A. Barthélémy and M. Bibes, *J. Phys.: Condens. Matter.*, 2014, **26**, 473201.

83. J. T. Heron, D. G. Schlom and R. Ramesh, *Appl. Phys. Rev.*, 2014, **1**, 021303.

84. J. C. Yang, Q. He, P. Yu and Y. H. Chu, *Annu. Rev. Mater. Res.*, 2015, **45**, 249.

85. J. Wu, Z. Fan, D. Xiao, J. Zhu and J. Wang, *Prog. Mater. Sci.*, 2016, **84**, 335.

86. S. Ning, S. C. Huberman, C. Zhang, Z. Zhang, G. Chen and C. A. Ross, *Phys. Rev. Appl.*, 2017, **8**, 054049.

87. Y.-H. Chu, M. P. Cruz, C.-H. Yang, L. W. Martin, P.-L. Yang, J.-X. Zhang, K. Lee, P. Yu, L.-Q. Chen and R. Ramesh, *Adv. Mater.*, 2007, **19**, 2662.

88. H. Béa, B. Dupé, S. Fusil, R. Mattana, E. Jacquet, B. Warot-Fonrose, F. Wilhelm, A. Rogalev, S. Petit, V. Cros, A. Anane, F. Petroff, K. Bouzehouane, G. Geneste, B. Dkhil, S. Lisenkov, I. Ponomareva, L. Bellaiche, M. Bibes and A. Barthélémy, *Phys. Rev. Lett.*, 2009, 102, 217603.

89. H. M. Christen, J. H. Nam, H. S. Kim, A. J. Hatt N. A. Spaldin, *Phys. Rev. B*, 2011, **83**, 144107.

90. C. Beekman, W. Siemons, T. Z. Ward, M. Chi, J. Howe, M. D. Biegalski, N. Balke, P. Maksymovych, A. Farrar and J. Romero, *Adv. Mater.*, 2013, **25**, 5561.

91. C.-H. Chiu, W.-I. Liang, C.-W. Huang, J.-Y. Chen, Y.-Y. Liu, J.-Y. Li, C.-L. Hsin, Y.-H. Chu and W.-W.Wu, *Nano Energy*, 2015, **17**, 72.

92. P. C. Dorsey, P. Lubitz, D. B. Chrisey and J. S. Horwitz, *J. Appl. Phys.*, 1996, **79**, 6338.

93. A. Lisfi, C. M. Williams, L. T. Nguyen, J. C. Lodder, A. Coleman, H. Corcoran, A. Johnson, P. Chang, A. Kumar and W. Morgan, *Phys. Rev. B*, 2007, **76**, 054405.

94. G. Hu, J. H. Choi, C. B. Eom, V. G. Harris and Y. Suzuki, *Phys. Rev. B*, 2000, **62**, R779.

95. A. Lisfi and C. M. Williams, *J. Appl. Phys.*, 2003, **93**, 8143.

96. W. Huang, J. Zhu, H. Z. Zeng, X. H. Wei, Y. Zhang and Y. R. Li, *Appl. Phys. Lett.*, 2006, **89**, 262506.

97. P.D. Thang, G. Rijnders and D.H.A. Blank, *J. Magn. Magn. Mater.*, 2007, **310**, 2621.

98. T. Dhakal, D. Mukherjee, R. Hyde, P. Mukherjee, M. H. Phan, H. Srikanth and S. Witanachchi, *J. Appl. Phys.*, 2010, **107**, 053914.

99. F. Eskandari, S. B. Porter, M. Venkatesan, P. Kameli, K. Rode and J. M. D. Coey, *Phys. Rev. Materials*, 2017, **1**, 074413.

100. Y.-M. Kang, S. H. Lee, T. C. Kim, J. Jeong, D. Yang, K.-S. Han and D. H. Kim, *Appl. Phys. A*, 2017, **123**, 648.

101. H. Zheng, F. Straub, Q. Zhan, P. L. Yang, W. K. Hsieh, F. Zavaliche, Y.-H. Chu, U. Dahmen and R. Ramesh, *Adv. Mater.,* 2006, **18**, 2747.

102. H. Zheng, J. Wang, L. Mohaddes-Ardabili, M. Wuttig, L. Salamanca-Riba, D. G. Schlom and R. Ramesh, *Appl. Phys. Lett.*, 2004, **85**, 2035.

103. Z. Wang, Y. Li, R. Viswan, B. Hu, V. G. Harris, J. Li and D. Viehland, *ACS Nano*, 2013, **7**, 3447.

104. S.-C. Liao, P.-Y. Tsai, C.-W. Liang, H.-J. Liu, J.-C. Yang, S.-J. Lin, C.-H. Lai and Y.-H. Chu, *ACS Nano*, 2011, **5**, 4118.

105. R. J. Zeches, M. D. Rossell, J. X. Zhang, A. J. Hatt, Q. He, C.-H. Yang, A. Kumar, C. H. Wang, A. Melville, C. Adamo, G. Sheng, Y.-H. Chu, J. F. Ihlefeld, R. Erni, C. Ederer, V. Gopalan, L. Q. Chen, D. G. Schlom, N. A. Spaldin, L. W. Martin and R. Ramesh, *Science*, 2009, **326**, 977.

106. T. Amrillah, S. K. Vandrangi, Y. Bitla, T. H. Do, S.-C. Liao, C.-Y. Tsai, Y.-Y. Chin, Y.-T. Liu, M.-L. Lin, Q. He, H.-J. Lin, H.-Y. Lee, C.-H. Lai, E. Arenholz, J.-Y. Juang and Y.-H. Chu, *Nanoscale,* 2016, **8**, 8847.

107. N. Dix, R. Muralidharan, J.-M. Rebled, S. Estradé, F. Peiró, M. Varela, J. Fontcuberta and F. Sánchez, *ACS Nano*, 2010, **4**, 4955.

108. N. Dix, R. Muralidharan, B. Warot-Fonrose, M. Varela, F. Sánchez and J. Fontcuberta, *Chem. Mater.*, 2009, **21**, 1375.

109. D. Chen, Z. Chen, Q. He, J. D. Clarkson, C. R. Serrao, A. K. Yadav, M. E. Nowakowski, Z. Fan, L. You, X. Gao, D. Zeng, L. Chen, A. Y. Borisevich, S. Salahuddin, J.-M. Liu and J. Bokor, *Nano Lett.*, 2017, **17**, 486.

110. H. Zheng, J. Kreisel, Y.-H. Chu, R. Ramesh and L. Salamanca-Riba, *Appl. Phys. Lett.*, 2007, **90**, 113113.

111. S. Park, M. S. Kim, J. Yang, T. C. Kim, S. H. Han and D. H. Kim, *J. Nanosci. Nanotechnol.,* 2017, **17**, 3523.

112. D. H. Kim, X. Y. Sun, N. M. Aimon, J. J. Kim, M. J. Campion, H. L. Tuller, L. Kornblum, F. J. Walker, C. H. Ahn and C. A. Ross, *Adv. Func. Mater.*, 2015, **25**, 3091.

113. D. H. Kim, J. Yang, M. S. Kim and T. C. Kim, *J. Cryst. Growth*, 2016, **449**, 62.

114. H. Zhen, Q. Zhan, F. Zavaliche, M. Sherburne, F. Straub, M. P. Cruz, L.-Q. Chen, U. Dahmen and R. Ramesh, *Nano Lett.*, 2006, **6**, 1401.

115. R. Muralidharan, N. Dix, V. Skumryev, M. Varela, F. Sánchez and J. Fontcuberta, *J. Appl. Phys.,* 2008, **103**, 07E301.

116. J. E. Greene, J. *Vac. Sci. Technol*. A, 2017, **35**, 05C204-1.

117. J. J. Thomson, *Philos. Mag.*, 1891, **32**, 321.

118. S. Swann, *Phys. Technol.*, 1988, **19**, 67.

119. K. Char, A. D. Kent, A. Kapitulnik, M. R. Beasley, T. H. Geballe, *Appl. Phys. Lett.*, 1987, **51**, 1370.

120. C. B. Eom, J. Z. Sun, K. Yamamoto, A. F. Marshall, K. E. Luther, T. H. Geballe and S. S. Laderman, *Appl. Phys. Lett.*, 1989, **55**, 595.

121. S. B. Krupanidhi, N. Maffei, M. Sayer and K. El-Assal, *J. Appl. Phys.*, 1983, **54**, 6601.

122. R. R. Das, D. M. Kim, S. H. Baek, C. B. Eom, F. Zavaliche, S. Y. Yang, R. Ramesh, Y. B. Chen, X. Q. Pan, X. Ke, M. S. Rzchowski and S. K. Streiffer, *Appl. Phys. Lett.*, 2006, **88**, 242904.

123. H. Sato, S. Tajima, H. Takagi and S. Uchida, *Nature*, 1989, **338**, 241.

124. A. Sharoni, J. G. Ramírez and I. K. Schuller, *Phys. Rev. Lett.*, 2008, **101**, 026404.

125. C. B. Eom, R. B. Van Dover, Julia M. Phillips, D. J. Werder, J. H. Marshall, C. H. Chen, R. J. Cava, R. M. Fleming and D. K. Fork, *Appl. Phys. Lett.*, 1993, **63**, 2570.
126. D. H. Kim, N. G. Cho, H.-G. Kim and W. Y. Choi, *J. Electrochem. Soc.*, 2007, **154**, H939.
127. D. Song, A. G. Aberle and J. Xia, *Appl. Surf. Sci.*, 2002, **195**, 291.
128. S. Hirano, J. Kim and S. Srinivasan, *Electrochim. Acta*, 1997, **42**, 1587.
129. I. Kanno, S. Hayashi, R. Takayama and T. Hirao, *Appl. Phys. Lett.*, 1996, **68**, 328.
130. Y.-C. Liang, T.-B. Wu, H.-Y. Lee and Y.-W. Hsieh, *J. Appl. Phys.*, 2004, **96**, 584.
131. S. B. Desu, *J. Electrochem. Soc.*, 1993, **140**, 2981.
132. T. Yasumoto, N. Yanase, K. Abe and T. Kawakubo, *Jpn. J. Appl. Phys.*, 2000, **39**, 5369.
133. W. Zhang, F. Hu, H. Zhang and J. Ouyang, *Mater. Res. Bull.*, 2017, **95**, 23.
134. S. Lee, N. Fuhimura and T. Ito, *Jpn. J. Appl. Phys.*, 1995, **34**, 5168.
135. H. W. Jang, D. Ortiz, S.-H. Baek, C. M. Folkman, R. R. Das, P. Shafer, Y. Chen, C. T. Nelson, X. Pan, R. Ramesh and C. B. Eom, *Adv. Mater.*, 2009, **21**, 817.
136. C. Jin, H. Liu, P. Li, D. F. Kuang and H. L. Bai, *J. Appl. Phys.*, 2011, **110**, 013917.
137. H. Yanagihara, Y. Utsumi, T. Niizeki, J. Inoue and E. Kita, *J. Appl. Phys.*, 2014, **115**, 17A719.
138. P. Prieto, J. F. Marco, J. E. Prieto, S. Ruiz-Gomez, L. Perez, R. P. del Real, M. Vázquez and J. de la Figuera, *Appl. Surf. Sci.*, 2018, **436**, 1067.
139. R. Y. Zheng, J. Wang and S. Ramakrishna, *J. Appl. Phys.*, 2008, **104**, 034106.
140. J. Wu and J. Wang, *J. Appl. Phys.*, 2009, **105**, 124107.
141. N. Dix, V. Skumryev, V. Laukhin, L. Fàbrega, F. Sánchez and J. Fontcuberta, *Mater. Sci. Eng., B*, 2007, **144**, 127.
142. I. Fina, N. Dix, V. Laukhin, L. Fàbrega, F. Sánchez and J. Fontcuberta, *J. Magn. Magn. Mater.*, 2009, **321**, 1795.
143. I. Fina, N. Dix, L. Fàbrega, F. Sánchez and J. Fontcuberta, *Thin Solid Films*, 2010, **518**, 4634.
144. I. Fina, N. Dix, L. Fàbrega, F. Sánchez and J. Fontcuberta, *J. Appl. Phys.*, 2010, **108**, 034108.
145. Q. Yang, W. Zhang, M. Yuan, L. Kang, J. Feng, W. Pan and J. Ouyang, *Sci. Technol. Adv. Mater.*, 2014, **15**, 025003.
146. T. C. Kim, S. Ojha, G. Tian, S. H. Lee, H. K. Jung, J. W. Choi, L. Kornblum, F. J. Walker, C. H. Ahn, C. A. Ross and D. H. Kim, *J. Mater. Chem. C*, 2018, **6**, 5552.
147. T. C. Kim, S. H. Lee, H. K. Jung, Y. E. Kim, J. W. Choi, D. Yang and D. H. Kim, *J. Magn. Magn. Mater.*, 2019, **471**, 116.
148. S. H. Lee, G. Tian, T. C. Kim, H. K. Jung, J. W. Choi, F. J Walker, C. H. Ahn, C. A. Ross and D. H. Kim, *Nanotechnology*, 2019, **30**, 105601.

149. R. A. McKee, F. J. Walker, M. B. Nardelli, W. A. Shelton and G. M. Stocks, *Science*, 2003, **300**, 1726.

150. S. Y. Yang, Q. Zhan, P. L. Yang, M. P. Cruz, Y. H. Chu, R. Ramesh, Y. R. Wu, J. Singh, W. Tian and D. G. Schlom, *Appl. Phys. Lett.*, 2007, **91**, 022909.

151. L. Louahadj, D. Le Bourdais, L. Largeau, G. Agnus, L. Mazet, R. Bachelet, P. Regreny, D. Albertini, V. Pillard, C. Dubourdieu, B. Gautier, P. Lecoeur and G. Saint-Girons, *Appl. Phys. Lett.*, 2013, **103**, 212901.

152. A. A. Demkov and A. B. Posadas, *Integration of Functional Oxides with Semiconductors*, Springer, New York City, 2014.

153. L. Kornblum, M. D. Morales-Acosta, E. N. Jin, C. H. Ahn and F. J. Walker, *Adv. Mater. Interfaces*, 2015, **2**, 1500193.

154. M. Alexe, J. F. Scott, C. Curran, N. D. Zakharov, D. Hesse and A. Pignolet, *Appl. Phys. Lett.*, 1998, **73**, 1592.

155. Z. Hu, M. Li, S. Pu, X. Liu, B. Sebo, X. Zhao and S. Dong, *Appl. Phys. Lett.*, 2012, **100**, 252908.

156. M. Dekkers, M. D. Nguyen, R. Steenwelle, P. M. te Riele, D. H. A. Blank and G. Rijnders, *Appl. Phys. Lett.*, 2009, **95**, 012902.

157. J. Kreisel, M. C. Weber, N. Dix, F. Sánchez, P. A. Thomas and J. Fontcuberta, *Adv. Funct. Mater.*, 2012, **22**, 5044.

158. R. Bachelet, P. de Coux, B. Warot-Fonrose, V. Skumryev, J. Fontcuberta and F. Sánchez, *Thin Solid Films*, 2011, **519**, 5726.

159. M. P. Warusawithana, C. Cen, C. R. Sleasman, J. C. Woicik. Y. Li, L. F. Kourkoutis, J. A. Klug, H. Li, P. Ryan, L.-P. Wang, M. Bedzyk, D. A. Muller, L.-Q. Chen, J. Levy and D. G. Schlom, *Science*, 2009, **324**, 367.

160. J. W. Reiner, A. M. Kolpak, Y. Segal, K. F. Garrity, S. Ismail-Beigi, C. H. Ahn and F. J. Walker, *Adv. Mater.,* 2010, **22**, 2919.

161. R. A. McKee, F. J. Walker and M. F. Chisholm, *Phys. Rev. Lett.,* 1998, **81**, 3014.

162. S. Sawamura, N. Wakiya, N. Sakamoto, K. Shinozaki and H. Suzuki, *Jpn. J. Appl. Phys.*, 2008, **47**, 7603.

163. X. L. Lu, Y. Kim, S. Goetze, X. G. Li, S. N. Dong, P. Werner and M. Alexe, D. Hesse, *Nano Lett.*, 2011, **11**, 3202.

164. X. Lu, S. Dong, X.Li, M.Alexe, D. Hesse and Y. Hao, *Appl. Phys. Lett*., 2012, **101**, 222902.

165. G. Tian, F. Zhang, J. Yao, H. Fan, P. Li, Z. Li, X. Song, X. Zhang, M. Qin, M. Zeng, Z. Zhang, J. Yao, X. Gao and J. Liu, *ACS Nano*, 2016, **10**, 1025.

166. S. H. Xie, F. Y. Ma, Y. M. Liu and J. Y. Li, *Nanoscale*, 2011, **3**, 3152.
167. N. M. Aimon, D. H. Kim, X. Sun and C. A. Ross, *ACS Appl. Mater. Interfaces*, 2015, **7**, 2263.
168. S. S. Hong, J. H. Yu, D. Lu, A. F. Marshall, Y. Hikita, Y. Cui and H. Y. Hwang, *Sci. Adv.*, 2017, **3**, eaao5173.
169. D. J. Baek, D. Lu, Y. Hikita, H. Y. Hwang and L. F. Kourkoutis, *ACS Appl. Mater. Interfaces*, 2017, **9**, 54.
170. D. K. Lee, S. Kim, S. Oh, J.-Y. Choi, J.-L. Lee and H. K. Yu, *Sci. Rep.*, 2017, **7**, 8716.
171. D. K. Lee, T. S. Kim, J.-Y. Choi and H. K. Yu, *Cryst. Growth Des.*, 2018, **18**, 5295.
172. S. A. Lee, J.-Y. Hwang, E. S. Kim, S. W. Kim and W. S. Choi, *ACS Appl. Mater. Interfaces*, 2017, **9**, 3246.

Figure Captions

Figure 1. Strain-mediated coupling in composites consisting of a ferromagnetic (FM) and a ferroelectric (FE) layer. The top panel illustrates the direct ME effect. Lattice strain in the magnetostrictive material from an applied magnetic field is transferred to the FE layer and it induces surface charges (ΔQ) through the piezoelectric effect. The bottom panel illustrates the converse ME effect. Lattice strain in the piezoelectric material from an applied electric field is transferred to FM layer and induces a magnetization change (ΔM) or domain reorientation in the FM layer.

Figure 2. Morphologies of BFO-CFO nanocomposites (volume fraction of 1:1) grown on **(a)** a (001) STO substrate at 700 °C, **(b)** a (111) STO substrate at 650 °C, and **(c)** a (110) STO substrate at 700 °C. (a) A plan-view bright-field TEM image showing rectangular CFO (bright) in a BFO (dark) matrix, a cross-sectional TEM image, and a high-resolution TEM image from the interface region. **(b)** A plan-view bright-field TEM image showing triangular BFO (dark) in a CFO (bright) matrix, a cross-sectional TEM image, and a high-resolution TEM image from the interface region. **(c)** A plan-view bright field TEM image showing a maze pattern of BFO (dark) and CFO (bright) and the corresponding cross-sectional TEM image. Reprinted with permission from ref. 101. Copyright 2006, John Wiley and Sons. **(d)** Plan view TEM image of the film grown at 920 °C, in-plane high resolution TEM image of one CFO pillar embedded in the BTO matrix grown at 950 °C, and magnified segment of the interface between the CFO pillar and the BTO matrix. Reprinted with permission from ref. 102. Copyright 2004, AIP Publishing.

Figure 3. Schematic of phase architectures and SEM images for differently oriented BFO-CFO thin films on **(a)** (001), **(b)** (110), and **(c)** (111) STO substrates with square, stripe, and triangular CFO features, respectively. Reprinted with permission from ref. 103. Copyright 2013, American Chemical Society. Schematics of morphology and AFM topography of BFO-CFO films grown on **(d)** DSO, **(e**) STO, and **(f)** NGO substrates. Reprinted with permission from ref. 104. Copyright 2013, American Chemical Society.

Figure 4. (a) Top view SEM image of 30 nm thick nanocomposite-STCu film grown in vacuum and 650 °C substrate temperature. **(b)** Top view SEM image of nanocomposite-STCu film etched in ammonium hydroxide for 3 hours. Top view SEM image of 90 nm thick BFO–CFO nanocomposite on **(c)** single crystal (001) STO substrate and **(d)** ammonium hydroxide etched nanocomposite-STCu/(001) STO substrate. Inset in **(d)** is a SEM image of BFO–CFO nanocomposite on STCu/STO substrate after etching in dilute HCl solution for 120 s at room temperature. In-plane and out-of-plane magnetic hysteresis loops of BFO–CFO on (e) STO and (f) nanocomposite-STCu/STO substrate. Reprinted with permission from ref. 112. Copyright 2015, John Wiley and Sons.

Figure 5. (a) XRD reciprocal space maps around LAO (103) for BFO-CFO/LAO (001). **(b)** Magnetization hysteresis loops measured at room temperature with the field applied in-plane (circles) and out-of-plane (rhombi) for samples on LAO (001). Magnetization is normalized to the CFO volume fraction. Labels in each panel indicate remanence/saturation magnetization ratio for parallel and perpendicular applied field. Reprinted with permission from ref. 107. Copyright 2010, American Chemical Society. Room temperature measured in-plane and out-of-plane hysteresis loops of various thickness MFO pillars in a BFO matrix grown on different thicknesses of BFO-blocked BFO–CFO nanocomposite. The height of the MFO pillars was **(c), (f)** 80 nm; **(d), (g)** 120 nm; and **(e), (h)** 160 nm. The blocking layer of BFO was 35 nm in (c)-(e) while in (f)–(h) the BFO blocking layer was 20 nm and the CFO and MFO are in contact. The insets show the structures schematically. Reprinted with permission from ref. 17. Copyright 2013, John Wiley and Sons.

Figure 6. (a) P-E hysteresis loops of 200 nm BFO films on 0.8 ° and 4 ° miscut (001) STO. **(b)** Hysteresis loops of 600 nm thick (001), (101), and (111) oriented BFO films. The hysteresis loops were measured on capacitors with top electrode diameter of 200 nm. Reprinted with permission from ref. 122. Copyright 2006, AIP Publishing. **(c)** Ferroelectric hysteresis loop of the CFO/BFO heterostructure. **(d)** Magnetization as a function of the applied magnetic field for the CFO/BFO heterostructure and the CFO single-layered film. Reprinted with permission from ref. 139. Copyright 2008, AIP Publishing. **(e)** In-

plane M-H hysteresis loops of the BFO single layer thin films and BFO/CFO bilayered thin films with different BFO thicknesses. Inset is magnetization M_s and coercivity H_c as a function of CFO thickness. **(f)** Leakage current density of BFO single layer thin films and BFO/CFO bilayered thin films as a function of applied electric field. Reprinted with permission from ref. 140. Copyright 2009, AIP Publishing.

Figure 7. (a) Top view SEM image and **(b)** XRD pattern of the BFO–CFO nanocomposite grown on a Nb:STO substrate at 650 °C at 50 mTorr with an Ar :O_2 ratio of 1 : 9. **(c)** Room temperature magnetic hysteresis loops of the BFO–CFO nanocomposite grown at a high oxygen ratio. **(d)** Amplitude and phase of the BFO–CFO nanocomposite measured by piezoresponse force microscopy as a function of DC bias voltage. **(e)** Magnified XRD patterns of the BFO–CFO nanocomposites around the (001), (002) and (003) substrate peaks before and after etching for 1 and 3 min. A relaxed CFO peak, which overlaps with the strained (002) R-BFO, is clearly seen at 43.11˚ after removing BFO. Magnetic hysteresis loops of the BFO–CFO nanocomposite after etching to remove BFO for **(f)** 1 and **(g)** 3 min. [146]

Figure 8. Top-view SEM images of BFO-CFO nanocomposite thin films grown under an atmosphere of **(a)** pure Ar, Ar:O_2 ratio of **(b)** 2:1, and **(c)** 1:2 at a working pressure of 30 mTorr, RF power of 40 W, and substrate temperature of 650 °C. In-plane and out-of-plane magnetic hysteresis loops of nanocomposites grown under an atmosphere of **(d)** pure Ar, and Ar:O_2 ratio of **(e)** 2:1, and **(f)** 1:2. **(g)** Mapping of BFO phase formation and magnetic anisotropy as a function of growth rate for optimizing synthesis conditions for self-assembled oxide nanostructures. Reprinted with permission from ref. 147. Copyright 2019, Elsevier.

Figure 9. Top-view SEM images of CFO-BFO nanocomposite thin films on LSMO annealed at 600 °C with thickness **(a)** 20 nm and **(b)** 50 nm. In-plane and out-of-plane magnetic hysteresis loops of nanocomposites grown on **(c)** 20 nm and **(d)** 50 nm thick LSMO thin films. **(e)** Writing and rewriting in CFO-BFO nanocomposite on a 20 nm thick LSMO by applying ±10 V. **(f)** Amplitude and phase of CFO-BFO nanocomposite on 20 nm thick LSMO measured by piezoresponse force microscopy as a function of DC bias voltage. Reprinted with permission from ref. 148. Copyright 2019, IOP Publishing.

Figure 10. Top view SEM image of nanocomposite on **(a)** single crystal STO substrate, **(b)** smooth STF35/CeO_2/YSZ/Si, **(c)** rough STF35/CeO_2/YSZ/Si, and **(d)** STO/Si substrates. Scale bars correspond to 100 nm. Insets in (b), (c) and (d) are top view SEM images of STF35 and STO films before nanocomposite deposition at the same scale. The circled CFO pillars (c) are 45° rotated cube-on-cube

epitaxial growth on STF35. The schematic diagram of cube-on-cube and 45° rotated cube-on-cube epitaxial growth are shown in (c). Reprinted with permission from ref. 65. Copyright 2014, John Wiley and Sons. **(e)** Top view SEM image and **(f)** magnetic hysteresis loops of the BFO-CFO nanocomposite grown on the STO buffered Si substrate at 650 °C at 50 mTorr with an Ar :O_2 ratio of 1 : 4 using sputter. [146]

Figure 11. Flowchart for the fabrication process. **(i)** Deposition of CFO film by pulsed electron deposition. **(ii)** Deposition of amorphous Si capping layer using RF sputtering. **(iii)** Spin coating of sample with negative-tone e-beam resist. **(iv)** Patterning of pillars using e-beam lithography. **(v)** Reactive ion etching of Si cap. **(vi)** Ar ion etching of CFO film. **(vii)** Deposition of 1 nm thick BFO film by pulsed electron deposition. **(viii)** Codeposition of CFO and BFO using pulsed electron deposition to form an epitaxial nanocomposite. Reprinted with permission from ref. 26. Copyright 2011, American Chemical Society.

Figure 12. (a) Steps of the nucleation-induced process: **(i)** mask transfer on the substrate, **(ii)** deposition of CFO through the mask, **(iii)** formation of nucleation centers by removal of the hard mask, **(iv)** growth of the ordered multiferroic composite by deposition from a mixed target. **(b) (i)** Atomic force microscopy (AFM) phase image showing the perfect phase segregation of the BFO−CFO composite system. Ferroelectric and magnetic activity as revealed by local measurements: **(ii)** amplitude and **(iii)** out-of-plane phase piezoresponse force microscopy (PFM) signal **(iv)** magnetic force microscopy (MFM) phase signal with the superposition of the contour of the pillars taken from the amplitude image. Reprinted with permission from ref. 25. Copyright 2013, American Chemical Society. **(c)** A schematic flowchart for the fabrication procedure. **(d)** Measured effects of magnetic field on the piezoelectric properties for a BFO/CFO/SRO nanodot. The piezoresponse loops including **(i)** amplitude-voltage butterfly loop and **(ii)** phase-voltage hysteresis loops with and without applying a magnetic field of 3000 Oe. **(e)** Effect of electric field on the magnetization pattern for the nanodot array. **(i)** The AFM topology image, and **(ii)** the MFM micrograph superimposed with its corresponding 3d topography image. The selected area magnified MFM images superimposed with their 3d topography (square area A and area B in **(i)**) before and after applying electric fields of ±8.5 V bias voltages through a conductive AFM probe, which are presented in **(iii)** and **(iv)**. Reprinted with permission from ref. 165. Copyright 2016, American Chemical Society.

Figure 13. (a) Schematic illustration of the fabrication process of a templated BFO-CFO nanocomposite. **(i)** Self-assembled square symmetry microdomain array from polyisoprene-b-polystyrene-b-polyferrocenyldimethylsilane/polystyrene (PI-*b*-PS-*b*-PFS/PS) blend. **(ii)** Square array of holes was generated from PI microdomains via surface reconstruction in hexane. **(iii)** Residual polymer layer on the bottom of holes was removed by a short O_2 plasma, then the STO substrate was etched through the polymer mask by immersing in aqua regia. **(iv)** Square array of pits in the STO surface was revealed after removing the polymer template. **(v)** CFO nuclei were selectively grown in patterned pits. **(vi)** A thin BFO layer was deposited to cover the mesas. **(vii)** A thick BFO-CFO nanocomposite was deposited, guided by the thin BFO-CFO composite. **(b) (i)** SEM image of BFO-CFO nanocomposite. **(ii)** Tilted view SEM image of free-standing CFO pillars after selectively removing the BFO matrix. Red circle indicates a short CFO pillar. **(iii)** In-plane and out-of-plane magnetization hysteresis loops of templated BFO-CFO nanocomposite measured at room temperature. Reprinted with permission from ref. 28. Copyright 2014, American Chemical Society. **(c)** Schematic of the templating process for vertical nanocomposites of CFO spinel pillars in a BFO perovskite matrix. The lower images show example morphologies. From left to right: AFM of Nb:STO substrate after FIB, 60 nm period; AFM after etching, 80 nm period; SEM of CFO in pits, 60 nm period; SEM after BFO deposition, 75 nm period; and SEM after growth of the composite, 80 nm period. **(d)** SEM images of perovskite-spinel nanocomposites templated into square lattices with periods **(i)** 80 nm and **(ii)** 100 nm. **(iii)** Square lattice of BFO-$Co_{0.5}Ni_{0.5}Fe_2O_4$ with period 67 nm. **(iv)** Parallel BFO-MFO lines with period 75 nm. (the inset shows an SEM of the corresponding CFO seed layer) All scale bars correspond to 100nm. Reprinted with permission from ref. 27. Copyright 2014, John Wiley and Sons.

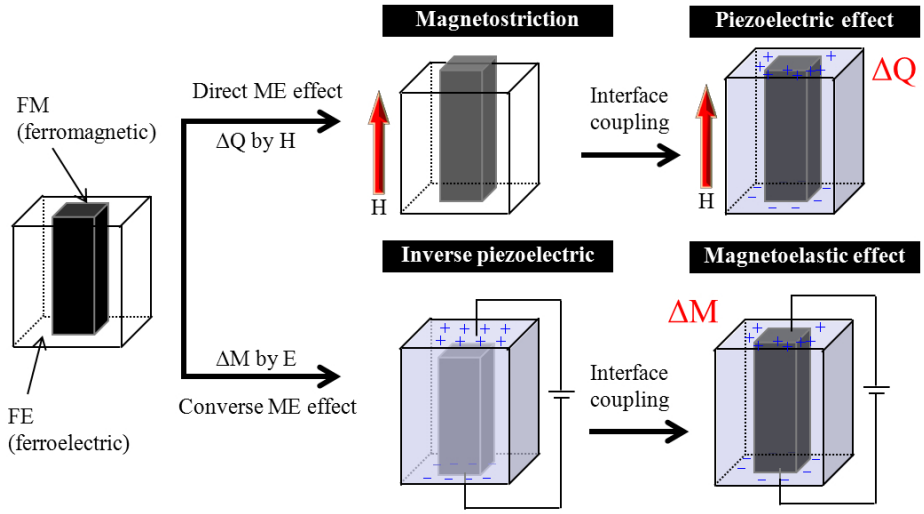

Fig.1

190x102mm (150 x 150 DPI)

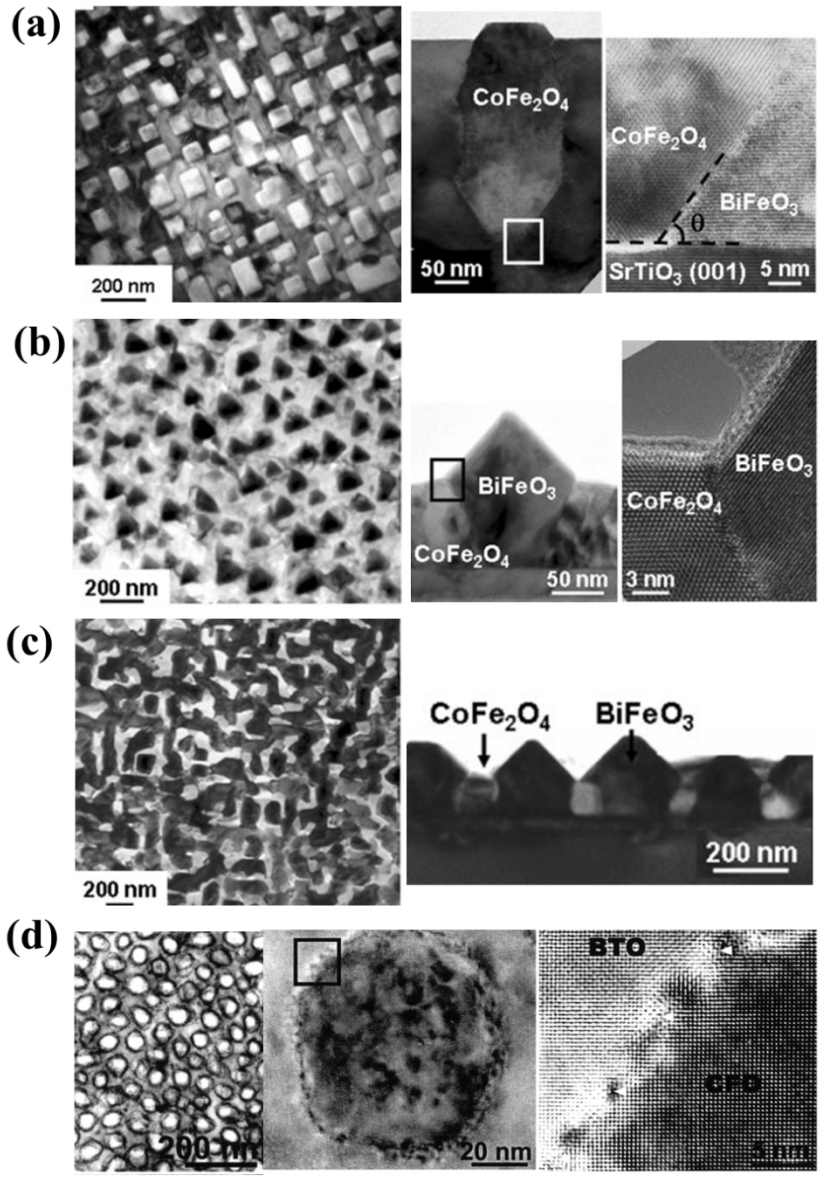

Fig. 2

170x235mm (150 x 150 DPI)

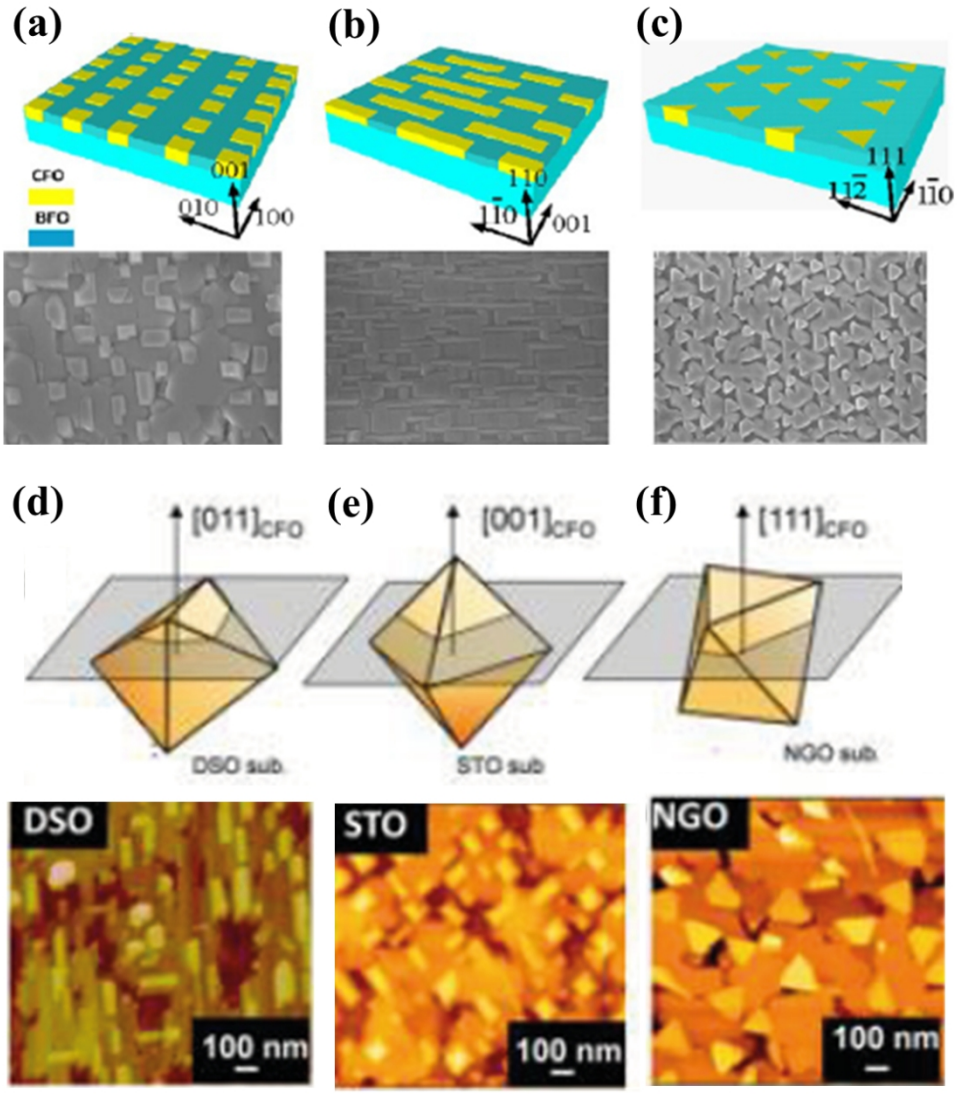

Fig. 3

197x227mm (150 x 150 DPI)

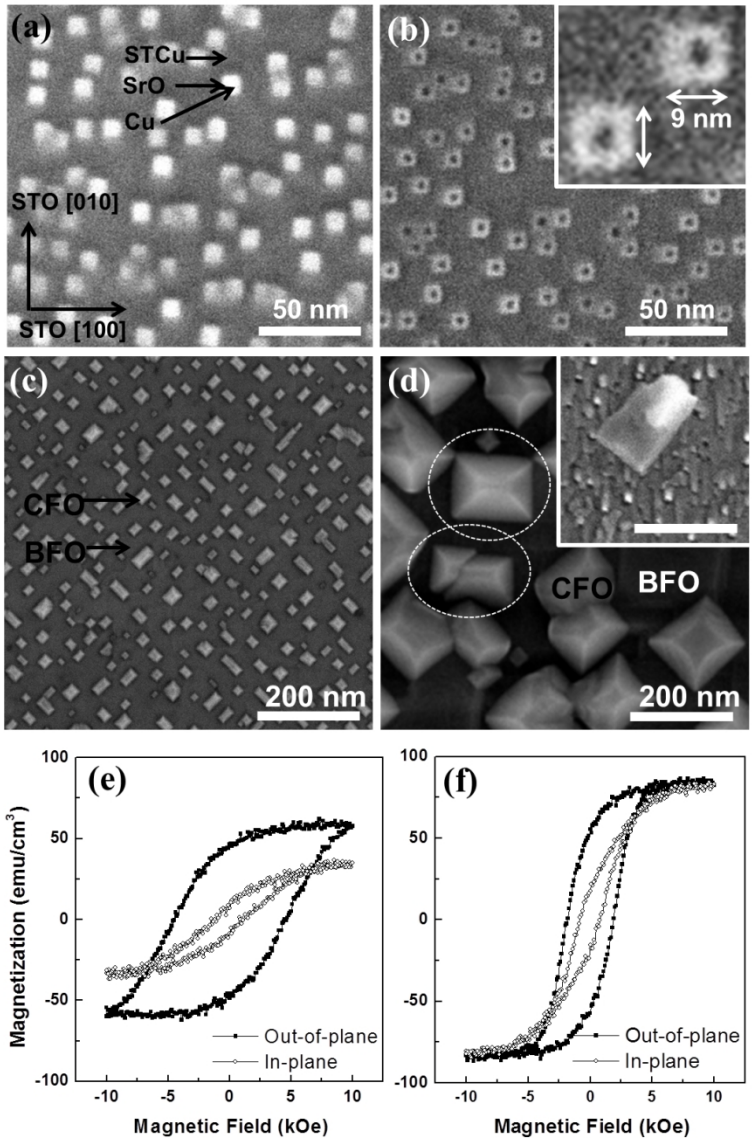

Fig. 4

203x287mm (150 x 150 DPI)

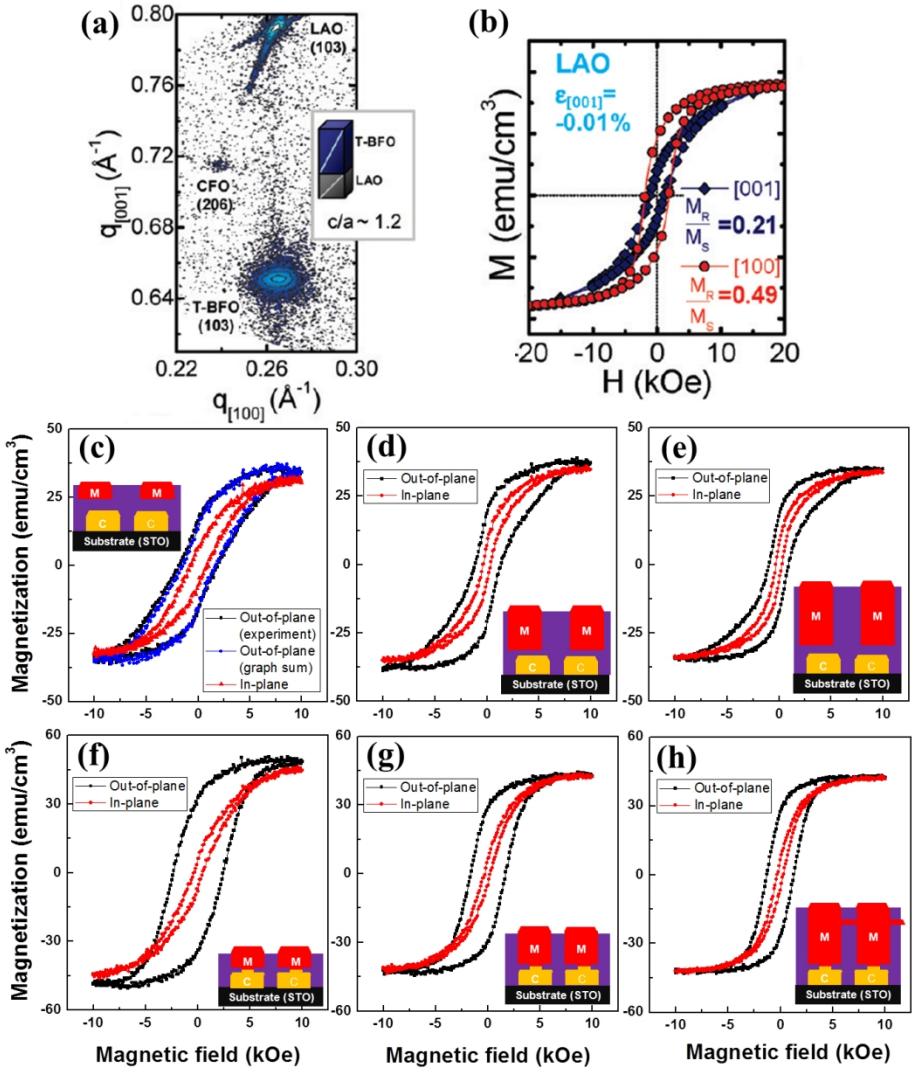

Fig. 5

253x282mm (150 x 150 DPI)

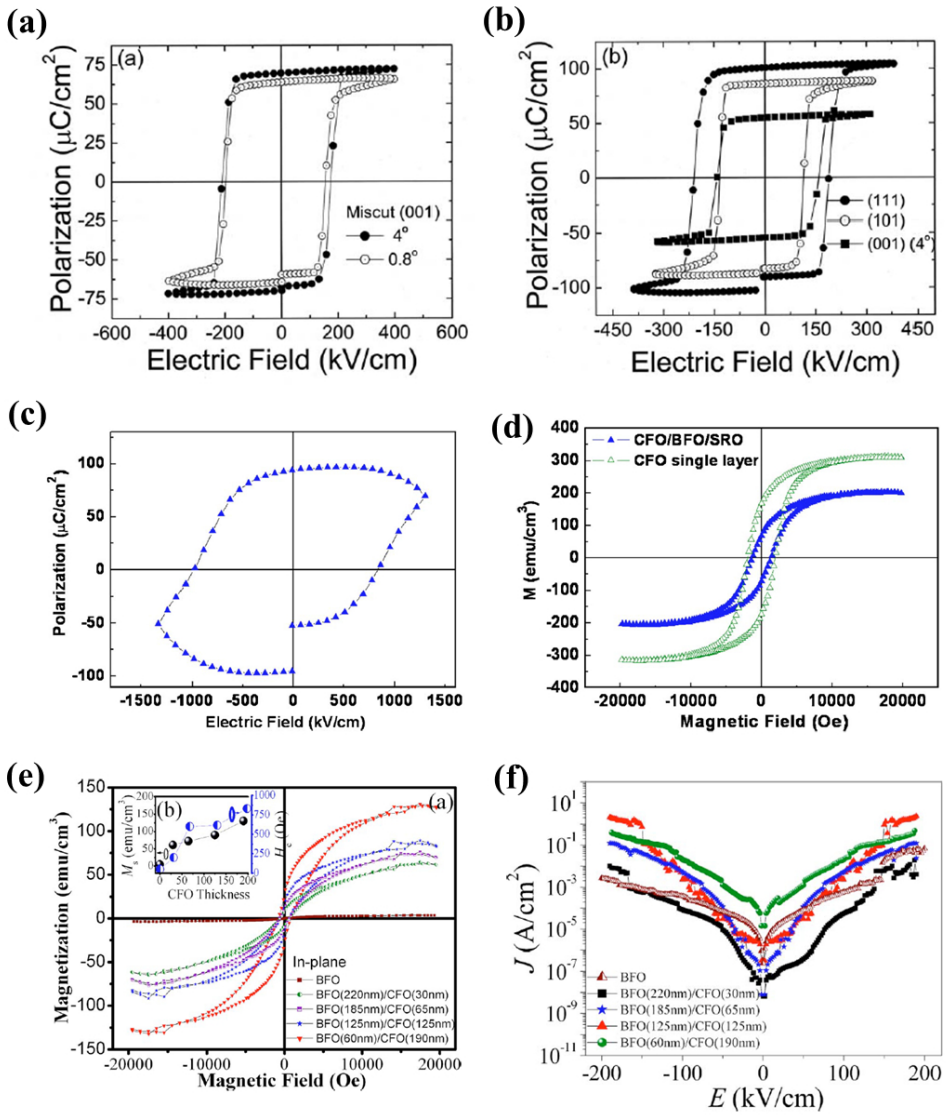

Fig. 6

182x214mm (150 x 150 DPI)

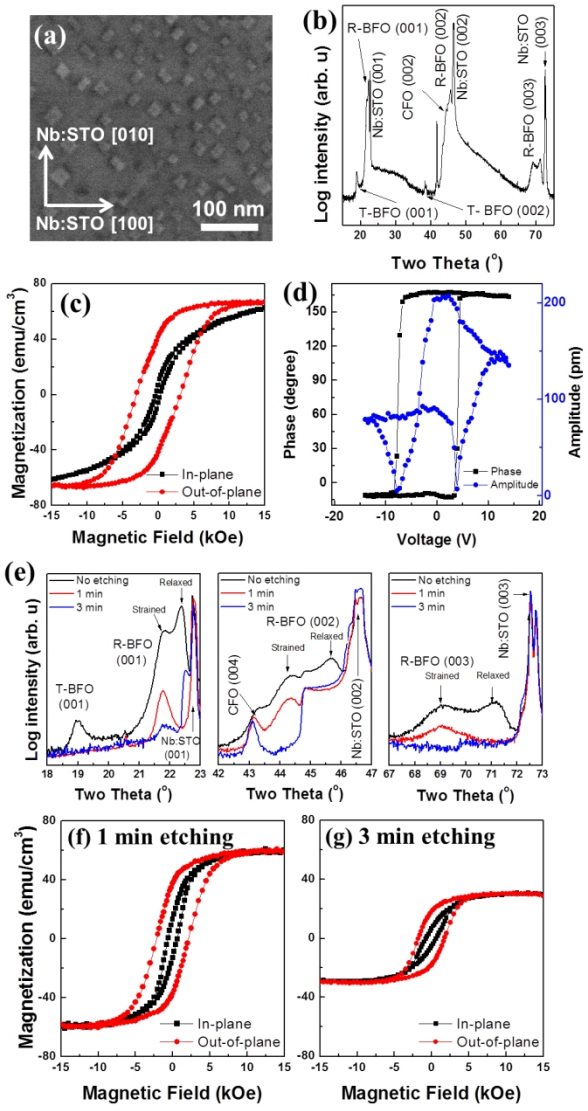

Fig. 7

192x358mm (150 x 150 DPI)

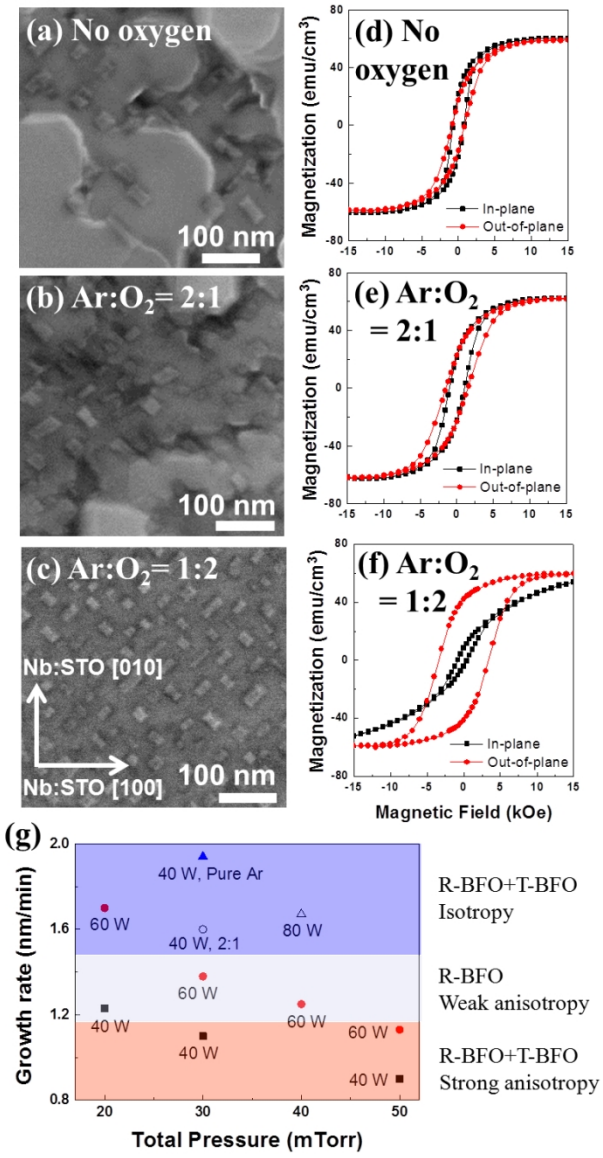

Fig. 8

149x265mm (150 x 150 DPI)

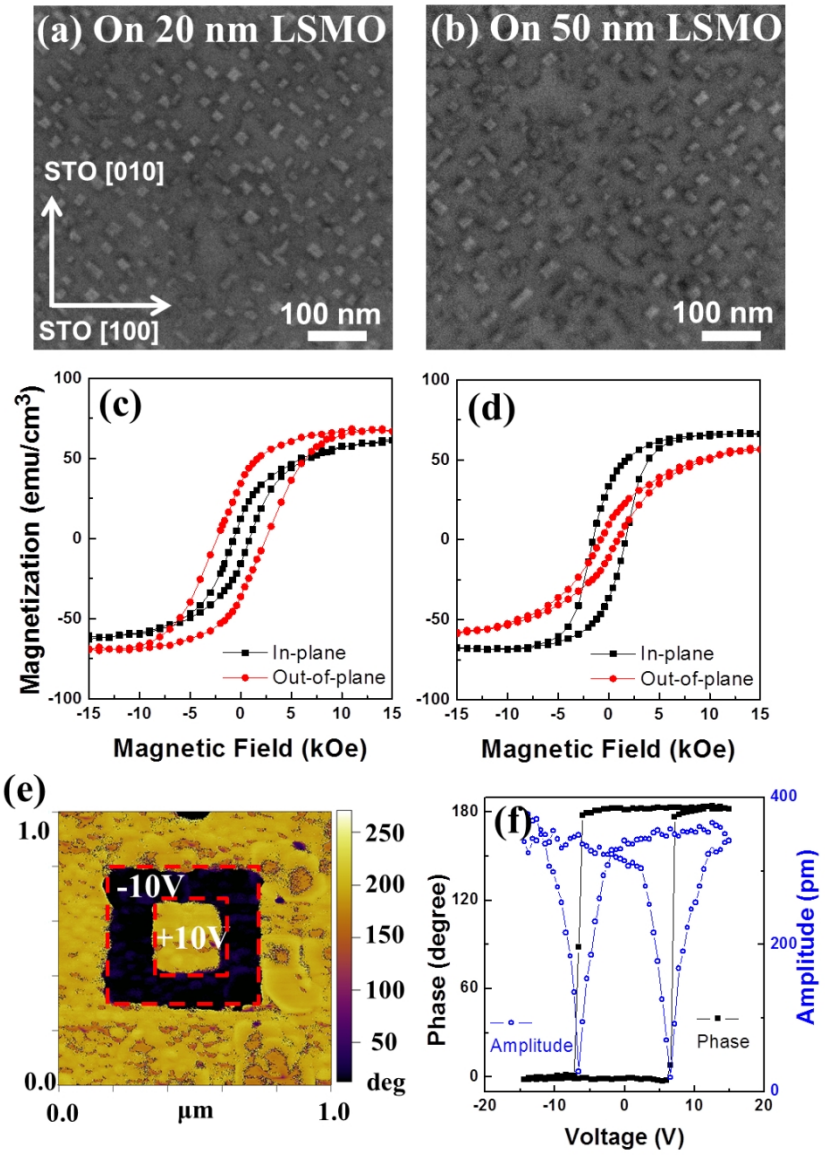

Fig. 9

188x256mm (150 x 150 DPI)

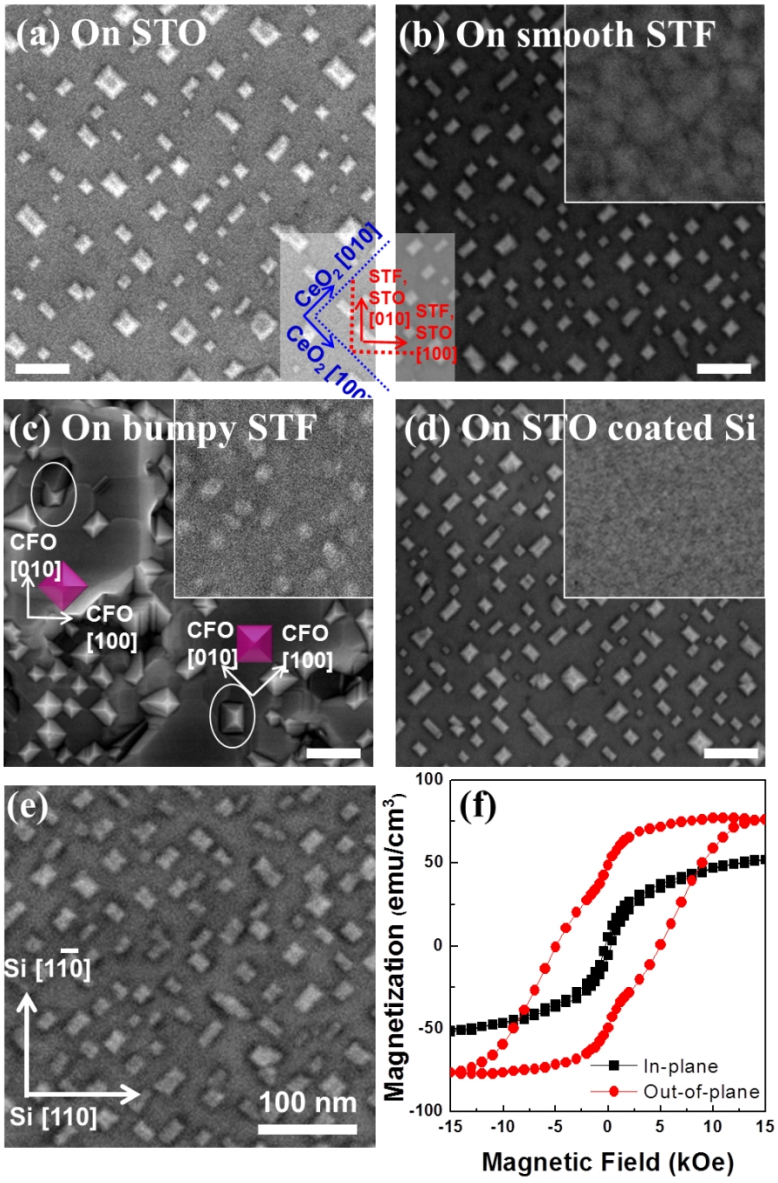

Fig. 10

190x263mm (150 x 150 DPI)

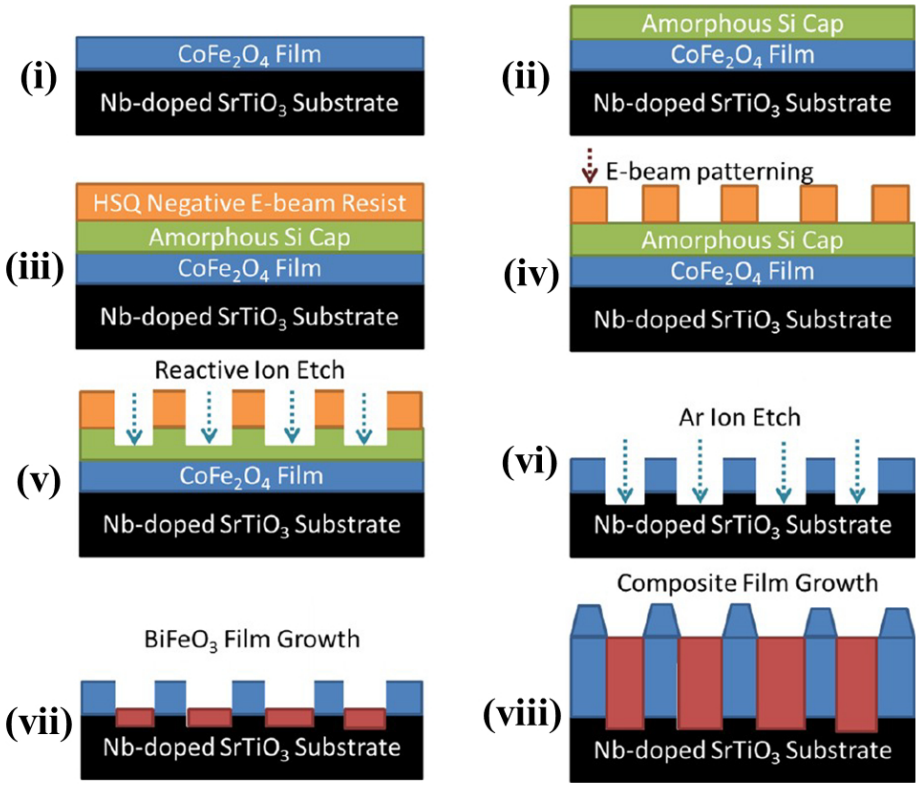

Fig. 11

177x146mm (150 x 150 DPI)

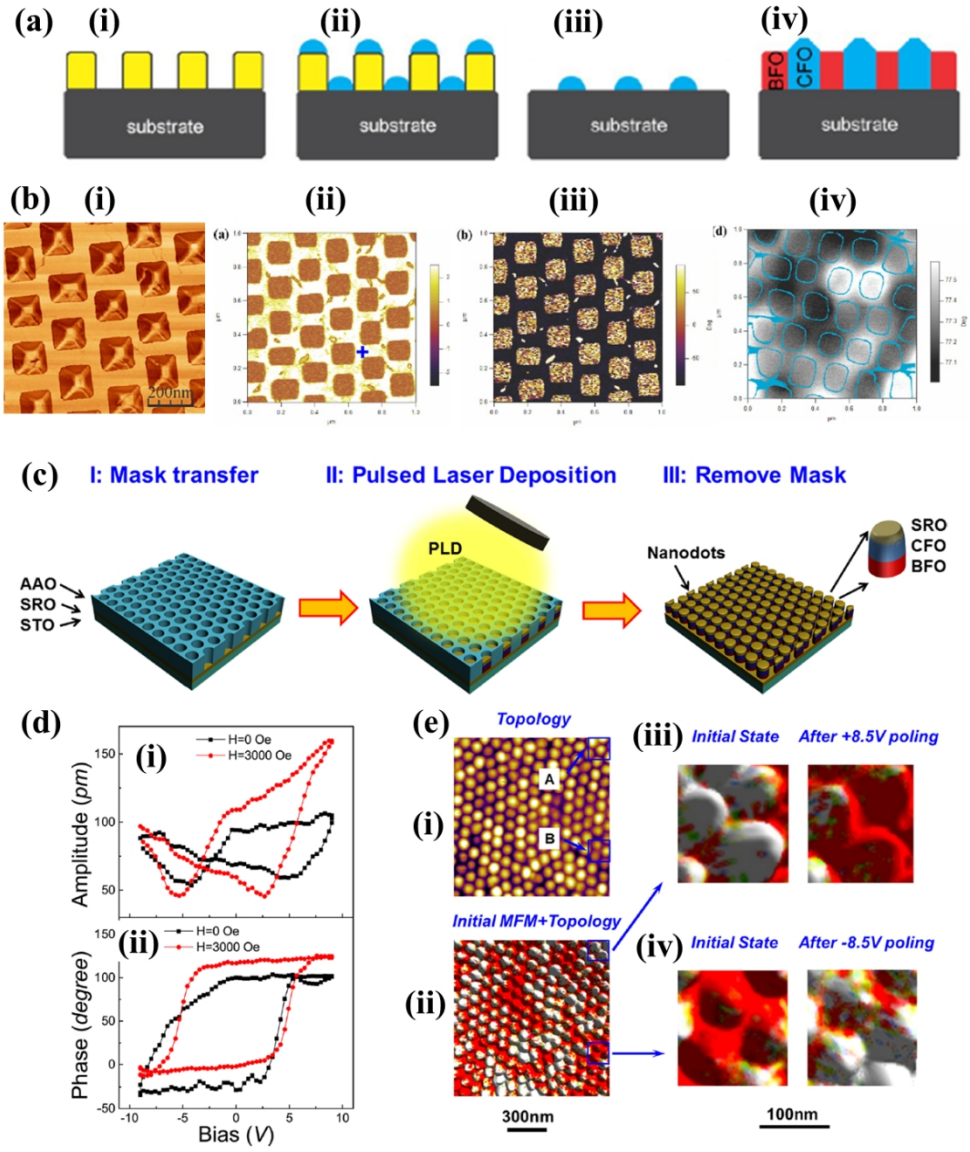

Fig. 12

210x252mm (150 x 150 DPI)

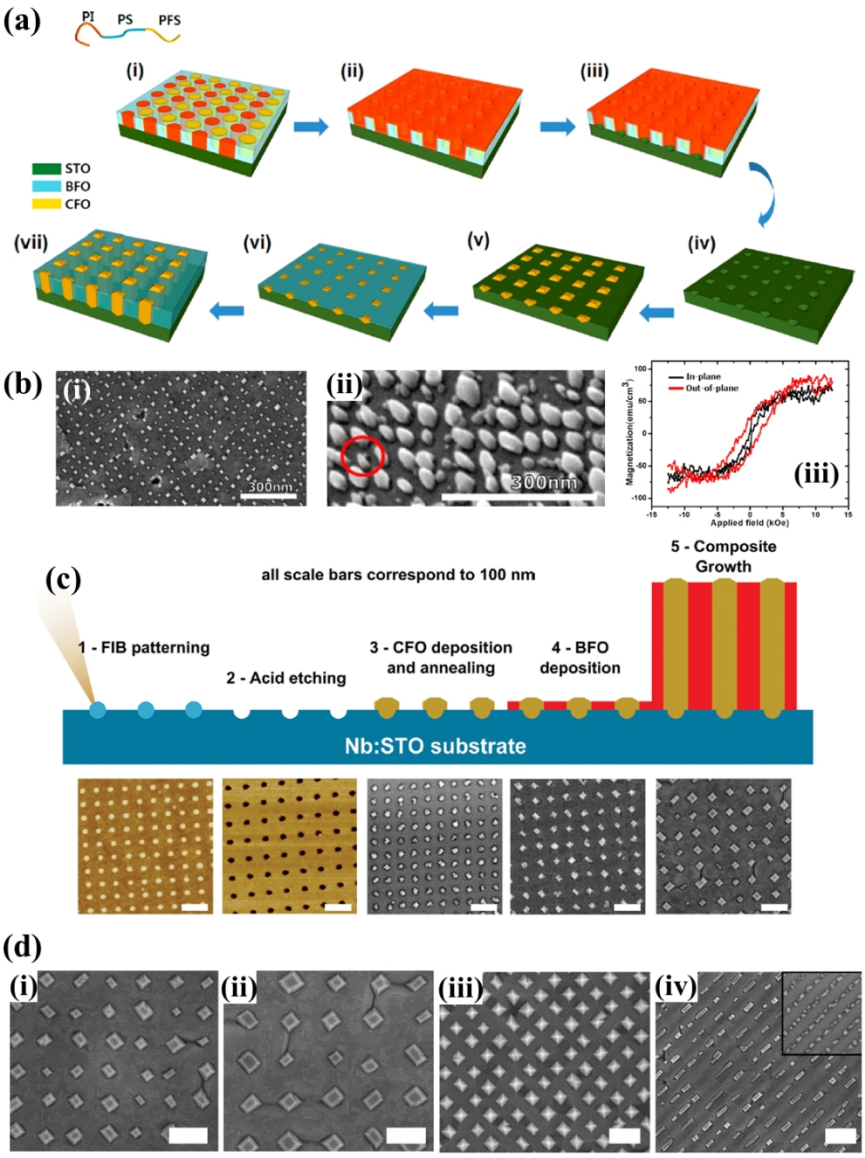

Fig. 13

195x258mm (150 x 150 DPI)

A table of contents entry

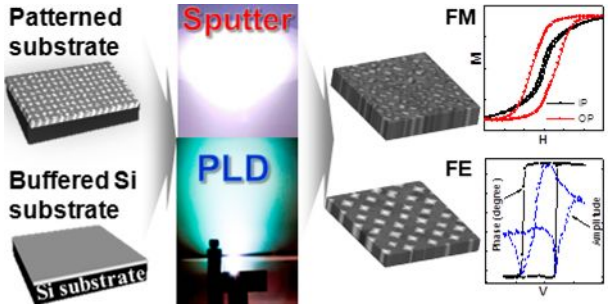

The recent progress on self-assembled epitaxial nanocomposites on silicon or templated substrates for low cost and large area devices.